2008

Design Methodology and Stability Analysis for a PhotoVoltaic (PV) Plant Interfaced with a • Distribution Network.

Prajna Paramita Dash
Western University

Design Methodology and Stability Analysis for a PhotoVoltaic (PV) Plant Interfaced with a Distribution Network.

(Spine title: Stability Analysis For A PV Plant))

(Thesis format: Monograph)

by

Prajna Paramita Dash

Graduate Program

in

Engineering Science

Department of Electrical and Computer Engineering

A thesis is submitted in partial fulfilment

of the requirements for the degree of

Master of Engineering Science

School of Graduate Studies and Postdoctoral Studies

The University of Western Ontario

London, Ontario, Canada

THE UNIVERSITY OF WESTERN ONTARIO

SCHOOL OF GRADUATE AND POSTDOCTORAL STUDIES

CERTIFICATE OF EXAMINATION

Supervisor	Examiners
Prof. Amirnaser Yazdani	Prof. Tarlochan S. Sidhu
	Prof. Ken McIsaac
	Prof. Amarjeet Bassi

The thesis by

Prajna Paramita Dash

entitled:

Design Methodology and Stability Analysis for A PhotoVoltaic (PV) Plant Interfaced With A Distribution Network

is accepted in partial fulfillment of the

requirements for the degree of

Master of Engineering Science

Date October 2, 2008

Prof. Roy Eagleson

Chair of the Thesis Examination Board

Abstract

In recent years, there has been significant interest in utilization of PhotoVoltaic (PV) solar systems of single- and double-digit MW power ratings, at sub-transmission and distribution voltage levels of the power system, under the umbrella of Distributed Generation (DG). Despite this interest, however, inadequate investigation has been dedicated to the connection of PV systems to distribution networks, and there is little experience regarding the operation of such PV systems. The study reported in this thesis attempts to address this gap.

This thesis proposes a control strategy and provides stability analysis for a typical single-stage, three-phase, PV system that is connected to a (residential/commercial) distribution network. The control is based on an inner current-control loop and an outer DC-link voltage regulator. The current-control strategy decouples the dynamics of the PV system from those of the network and the loads. The DC-link voltage control scheme enables the control and maximization of the output real power of the PV system. Further, a feed-forward control strategy is employed for the DC-link voltage regulation scheme, to enhance the stability of the PV system. The feed-forward compensation scheme makes the PV system dynamics independent of the nonlinear characteristic of the PV panels. This, in turn, permits the design and optimization of the PV system controllers for a wide range of operating conditions.

In this thesis, a mathematical model and a control design methodology are presented for the PV system, and it is shown that, under proposed control, the PV system fulfills the operational requirements for a grid-connected PV system. The effectiveness of the proposed control strategy and the most important transients of the PV system are evaluated through simulation studies conducted on a detailed switched model of the PV system, in the PSCAD/EMTDC software environment.

Based on the developed mathematical model, a modal/sensitivity analysis is conducted in this thesis on a linearized model of the overall system, i.e. the PV system, the distribution network, and the local loads, to characterize the dynamic properties, to evaluate the robustness of the controllers, and to identify the nature of interactions between the PV system and the network/loads. The modal analysis confirms that, under the proposed control strategy, dynamics of the PV system are decoupled from those of the distribution network/loads. This, alternatively, means that, if its controllers are designed based on the proposed structure and methodology, the PV system

does not destabilize the distribution network. It is also shown that the PV system dynamics are not influenced by those of the network. Thus, the PV system maintains its stability and dynamic properties despite major variations in the line length, line X/R ratio, load type, and load distance from the PV system.

Keywords- Distributed Generation (DG), PhotoVoltaic (PV) solar power, Voltage-Sourced Converter (VSC), power electronics, control, modal analysis, eigenvalue analysis, participation factor, feed-forward, distribution power network, modeling.

Acknowledgements

I would like to acknowledge my sincere and profound gratitude to Prof. Amirnaser Yazdani, for his invaluable supervision and encouragement throughout this research. In addition, financial support from Prof. Amirnaser Yazdani and Faculty of Engineering of the University of Western Ontario is gratefully acknowledged.

I would also like to thank my parents who have always been my source of inspiration.

Table of Contents

List of Tables

List of Figures

Nomenclature

v_t : VSC AC-side terminal voltage

v_s : VSC filtered voltage, the PCC voltage

v_l : Load voltage

v_g : Substation bus (Grid) voltage

v_{dc} : DC-link (PV matrix) voltage

i : VSC AC-side current

i_{g1} : Distribution line current between PCC and load

i_{g2} : Distribution line current between load and substation

i_l : Load current

i_{pv} : PV matrix current

P_{pv} : PV matrix power

P_s : Real power exchanged at the PCC

Q_s : Reactive power exchanged at the PCC

N : Interface transformer turns ratio

L : Inductance of VSC interface reactor

R : Resistance of VSC interface reactor

L_1 : Line inductance between PCC and load

L_2 : Line inductance between load and substation

R_1 : Line Resistance between PCC and load

R_2 : Line Resistance between load and substation

C : DC-link capacitance

C_f : Shunt capacitance at the PCC

C_l : Power-factor correction capacitance

ω : dq-frame angular speed

ω_0 :Nominal frequency of grid (e.g. 377 rad/s)

ρ : dq-frame reference angle

S : Insolation level

$Re\{\}$: Real part of

$Im\{\}$: Imaginary part of

$\tilde{}$: Superscript denoting small-signal perturbation of a variable

"0" : Subscript denoting steady-state value of a variable

$\hat{}$: Superscript denoting the peak value of a three-phase variable

"T" : Superscript denoting matrix transposition

s : Complex frequency, $\sigma + j\omega$

$\star$: sign for convolution between two terms

In this thesis, a Laplace-domain variable is signified by a capitalized first letter. For example, $£\{\omega\} = \Omega$, $£\{v_{sd}\} = V_{sd}$, etc.

Chapter 1

Introduction

1.1 Statement of the Problem and Thesis Objectives

In a PhotoVoltaic (PV) system, the conversion of solar energy to electricity is facilitated by means of an array of PV panels and a power-electronic converter system. This, in view of nonlinear characteristics of the PV panels and power conditioning unit, coexistent with a multi-loop control structure, raises concern about the dynamic behavior and impact on the distribution network of a PV system. Moreover, to most utility companies, grid-connected PV systems– and for that matter most of other Distributed Generation (DG) systems– are black boxes whose models are unknown and dynamic properties unidentified. Thus, adequately accurate models must be developed to enable impact studies and help the system transients be characterized. Such models must provide the capability of being augmented with those of the distribution networks, to allow comprehensive analytical and simulation studies. This, however, is not a straightforward task since manufacturers do not divulge design parameters or dynamic properties of their products, for proprietary reasons. Therefore, the only viable option seems to be that of the development of models that are based on the experts' understand-

ing of a typical PV system; such models might not exactly represent real-world PV systems, but will capture the essence of generally-accepted behavior of such systems. This is the overall objective of the work presented in this thesis. Specific objectives of this investigation are:

- to formulate a mathematical model as well as a simulation model for a typical PV system connected to a distribution power network;
- to propose a control design methodology for the PV system, such that the functionality of the PV system based on the developed model agrees with that generally understood and accepted for a typical, real-world, grid-connected, PV system;
- to characterize the most important transients and the behavior of the PV system in response to various disturbances; and
- to investigate stability and to identify dynamic properties of the PV system, especially, in view of the connection to a distribution power network and proximity to regional loads.

1.2 Background

In recent years, lack of adequate transmission capacity, limitation in constructing new transmission lines, and electricity market deregulation have been the main driving forces behind the concept of Distributed Generation (DG) whereby small-scale generators can be permitted at the distribution level and close to the end users [1]. Many DG systems employ renewable resources for electricity generation and therefore help the mitigation of adverse environmental impacts

of the fossil-fuel-based centralized generation. Among renewable DG systems, PV solar systems have attracted considerable attention and investment in several countries; and despite its relatively high cost and low efficiency, significant progress and penetration of the PV energy is forecasted. In fact, in each of the years 2001 and 2002, the world PV production grew by 40% per annum, bringing total world PV production in 2002 to an estimated 560 MW [4]. Appreciable progress in increasing the efficiency and reducing the cost of PV energy has been made over the past few decades. Thus, commercially available PV modules now have 20% efficiency as compared to 17% in the last decade, and the PV modules price has dropped to below $4 per peak Watt. Since, the energy source in a PV system is pollution-free, most abundantly available, and operable for a relatively long time without wearing out, many commercial and industrial buildings now have PV arrays that supply a substantial proportion of their energy needs, and megawatt-sized PV power stations are connected to the electricity grid and are in operation. Such an aggressive growth of the distributed PV generation may entail undesirable consequences for the existing power system, in terms of harmonics, voltage profile, stability, etc. Therefore thorough investigations are required in terms of modeling, control, and performance of the PV systems.

Thus far, PV systems of single- or double-digit MW capacities have been connected to the power system at sub-transmission voltage levels. However, there exists little experience on the interconnection of such PV systems with distribution networks, where load and/or other local generators are also present. Research on the PV systems in the context of DG is still in beginning stage. Presently, DG PV systems are mainly composed of single-phase, rooftop installations, with capacities limited to few hundred Watts, which are unlikely to make an impression on

the distribution network and the loads. Such PV systems are not even permitted to cause a reverse power flow. This is however not true for large-scale PV systems which have considerably higher capacities and more sophisticated control. Thus, it is imperative to analyze larger-scale, three-phase, PV systems employed as DG units, in terms of their control, dynamic characteristics, and performance.

There exists a vast body of the technical literature that deals with different aspects of PV systems including energy production and economics [5]- [7]. The most widely-addressed engineering issue regarding a PV system is the so-called Maximum Power-Point Tracking (MPPT). Reference [8] reviews 19 different MPPT methods introduced since 1968. The scope of the reported literature encompasses both large-scale and DG PV systems. Another widely-addressed topic is that of power converter configurations and aggregation schemes for PV systems. References [9]- [12] provide comprehensive reviews on different single-phase and three-phase converter circuits for PV applications. Recently, with the consideration of PV systems as DG units, the literature has also reported the integration of islanding detection schemes into single-phase PV systems [13]- [16]. In addition, a fair amount of the technical literature has dealt with the integration of PV systems into distribution networks. Majority of this body of the literature has focussed on single-phase PV systems, with an emphasis on harmonic interferences with the distribution networks [17]- [19] and on the power quality [20]- [22]. However, only a few previous works have investigated the control and stability aspects of PV systems.

Dynamic stability of single-phase, DG, PV systems is investigated in a number of works [23]- [24]. The work in [23] has conducted an eigenvalue analysis for a two-stage configuration with the model of the DC cable between the

two stages considered. However, the distribution line and loads are not modeled. Reference [24] has studied the impact of grid impedance variation on the closed-loop stability of a single-phase PV system. Moreover, a control design methodology to ensure the provision of adequate damping has been presented. A number of works have studied dynamic models, stability, and/or control of three-phase, single-stage, PV systems [27]- [30]. Reference [27] has elegantly developed a reduced-order model for a PV system which can be conveniently incorporated into power system time-domain simulations. However, the control approach proposed in [27] is a voltage-mode control strategy, which is prone to protection complication when the PV system is faulted. Moreover, no controller design methodology has been presented in [27]. A number of literatures, [28]-[30], have adopted the current-mode control strategy. Reference [28] identifies the control loops and the transfer-functions of a PV system. However, it reports no analysis of the stability or interactions, especially with regards to the line/loads. The work presented in [29] has adopted a similar analysis approach as in [28], investigating the impact of grid impedance on the closed-loop stability. However, the interaction between the PV system and the distribution network has not been studied. In [30] the behavior of a three-phase, single-stage, PV system has been studied. However, the emphasis is on the MPPT strategy, rather than on the control or stability of the PV system.

1.3 Methodology and Software Used

The research carried out in this investigation proposes a new control strategy for a single-stage, three-phase, PV system which is connected to a power distribu-

tion network. The proposed control strategy is based on a modified version of the conventional current-mode control and is used to (i) regulate the PV system power-factor (at unity, for example) and (ii) to control the PV system DC-link voltage and, therefore, its real-power output. In addition to protecting the PV system against external faults, the modified current-control strategy virtually decouples the PV system from the distribution network and the loads, as analytically shown in this thesis. On the other hand, the DC-link voltage control scheme ensures a stable operation of the PV system, guarantees safe operation of the power-conditioning unit of the PV system, and permits the incorporation of an MPPT scheme. This thesis also proposes a feed-forward compensation strategy for the DC-link voltage control loop, to eliminate the impact of nonlinearities of the PV panels on the closed-loop stability of the PV system. Thus, the proposed feed-forward compensation permits the design of the DC-link voltage controller irrespective of the PV system operating point, and also renders the closed-loop eigenvalues of the PV system insensitive to the DC-link voltage level and the solar irradiation. The effectiveness and robustness of the proposed control strategy against changes in the operating conditions, distribution network parameters, and load types/parameters are demonstrated through a comprehensive modal analysis as well as nonlinear, time-domain, simulation studies.

The modal analysis is conducted on a linearized mathematical model of the overall system, i.e. the system including the PV system, the power distribution network, and the loads, implemented in the MATLAB software environment. The simulation studies are, however, performed on a detailed, large-signal, circuit-based model of the overall system in the PSCAD/EMTDC software environment [31]. Thus, in the absence of an experimental set-up, the PSCAD model– to

which we refer to as the "detailed switched model" in this thesis– serves as an effective, reliable means of further evaluation of the proposed control strategy and the transient behavior of the overall system.

PSCAD is an effective, popular simulation tool for simulation of complex power systems which may have a fair degree of complexity in the control, switching, etc. PSCAD provides large-signal, electromagnetic transients, time-domain instantaneous responses, and various analysis tools. Therefore, it provides an economical substitution for hardware implementations where the power/voltage ratings are significant. The PSCAD is, however, not capable of identifying and quantifying the cause and nature of control instabilities and dynamic interactions among different system components. Such information can be obtained only through analytical methods, e.g. eigenvalue analysis.

1.4 Thesis Outline

The thesis consists of six chapters:

- in Chapter 2, first, a mathematical model of the PV system connected to a stiff grid is developed both in space-phasor and dq-frame domains. Based on the developed model, the DC-link voltage control and the AC-side current-control schemes are designed. Moreover, a feed-forward compensation strategy is proposed for the DC-link voltage control. Furthermore, a few case studies are carried out to validate the model.

- Chapter 3 augments the model developed in Chapter 2 with that of a distribution network. Chapter 3 also considers an asynchronous machine load connected to the distribution network. The mathematical model of the dis-

tribution network and the load are also presented in detail. Moreover, the performance of the PV system is evaluated and the most important transients are identified through simulation studies.

- Chapter 4 deals with the small-signal stability and eigenvalue analyses of the overall system, consisting of the PV system, the distribution network, and the load. In this Chapter, the nonlinear equations of the system are linearized around an equilibrium point, and the responses obtained from the linearized model are compared with those obtained from detailed switched model of the system to verify the linearized model. Then, an eigenvalue analysis is carried out on the linearized model to characterize the dynamics of the PV system, to identify the nature of interactions between the PV system and the network/loads, and to determine the robustness of the PV system control against variations of the parameters.

- In Chapter 5, performance of the PV system is studied in the presence of different kinds of loads to demonstrate if the proposed PV system maintains its stability and dynamic properties irrespective of load types. Chapter 5 quantifies the stability of the PV system in terms of eigenvalues.

- Chapter 6 concludes the thesis, and provides suggestions for future research.

1.5 Contributions

The main contributions of this thesis are:

- a new control strategy for a single-stage, three-phase, PV system is proposed. The proposed control strategy is based on a modified version of the

conventional current-mode control and is used to (i) regulate the PV system power factor and (ii) to control the converter DC-link voltage and, therefore, the PV system real power, through a voltage control scheme. In addition to protecting the PV system against faults, the modified current-control strategy virtually decouples the PV system from the distribution network and the load.

- Based on the developed dynamic model and control strategy, important transients are identified through simulation in PSCAD/EMTDC environment when the proposed PV system is interfaced with a distribution network and a load is connected to the distribution network.

- A feed-forward compensation strategy for DC-link voltage control loop has been proposed to eliminate the nonlinear characteristic of the PV panel. Thus, the proposed feed-forward compensation permits the design of the DC-link voltage controller irrespective of the PV system operating point.

- A linearized model of the PV system in conjunction with the distribution network and load is developed. An eigenvalue analysis on the linearized model is carried out to identify the nature of interactions between the PV system dynamics and those of networks/loads, and to determine the robustness of the proposed control against variation of parameters.

Chapter 2

Modeling and Control of a PhotoVoltaic (PV) Plant Interfaced with a Stiff Grid

2.1 Introduction

This chapter develops a mathematical model and identifies the controllers of a PhotoVoltaic (PV) system that is interfaced with a stiff grid. Thus, the stiff grid is modeled by an ideal, three-phase, voltage source. This enables the modeling and analysis of the PV system independent of dynamic properties of the distribution network and loads. Similarly, the controllers of the PV system are designed in this chapter under the assumption that the PV system is not affected by the distribution network to which it is connected. The developed model will be augmented with that of a distribution network in Chapter 3, to constitute a mathematical model for the overall system, and to enable the study of interactions between the PV system and the distribution network.

In this chapter, based on the PV system model, a controller is designed to regulate the DC-link voltage of the Voltage-Sourced Converter (VSC) such that the power out of the PV panel can be maximized in varying weather conditions.

In this chapter, a feed-forward compensation mechanism is proposed for DC-link voltage control loop. Fast and decoupled controller for d- and q- components of the VSC AC-side currents are also derived. Finally, performance of the PV system is evaluated by simulation case studies. Thus, a few case-studies are performed to demonstrate the effectiveness of the feed-forward compensation of the DC-link voltage control scheme.

This chapter is organized as follows: Section 2.2 introduces the structure of a single-stage, three-phase, PV system. Sections 2.3 and 2.4 present the mathematical model and controllers of the PV system, respectively. Performance of the PV system under the proposed control strategy is evaluated in Section 2.5. Section 2.6 concludes the chapter.

2.2 Structure of PV System

Fig. 2.1 shows a single-line schematic diagram of a typical PV system that is interfaced with a stiff grid, represented by the voltage source v_g at a Point of Common Coupling (PCC). The main building blocks of the PV system are a matrix of PV panels, a forced-commutated VSC, a three-phase, LC, interface filter, and the interface transformer T_{r1}. The matrix of PV panel is composed of parallel combination of n_p number of strings. Each string is composed of n_s number of series-connected PV cells. The numbers n_p and n_s are chosen such that the PV matrix delivers an adequately large DC voltage and power. The PV matrix is connected in parallel with the DC-side terminals of the VSC. The DC-link capacitance of the VSC is represented by C. Each AC-side terminal of the VSC is interfaced with the corresponding phase of the low-voltage side of T_{r1}, through

one phase of the interface filter. Each phase of the filter is composed of a series reactor and a shunt capacitor. The inductance and resistance of the reactor are represented by L and R, respectively, and its capacitance is signified by C_f. C_f provides a low-impedance path for the current harmonics generated by the PV system and prevents them from penetrating into the grid. R also includes the effect of the VSC ohmic losses. The interface filter is employed to prevent voltage and current harmonics generated by the VSC from penetrating into the grid. P_s and Q_s, respectively, represent the real and reactive power that the PV system delivers to the grid at the PCC. The transformer T_{r1} steps down the network voltage to a level suitable for the PV system. The high-voltage side of T_{r1}, i.e. the side interfaced with the grid, has a star-connected winding configuration and is solidly grounded.

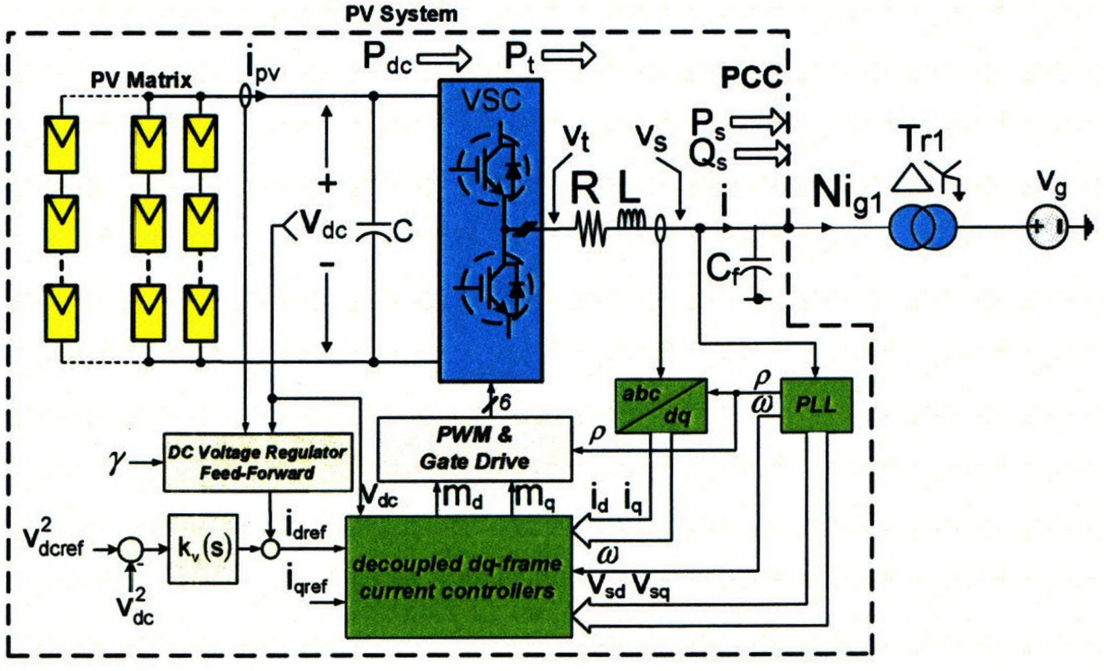

Figure 2.1: Single-line diagram of a typical PV system connected to a stiff grid

2.3 PV System Model

A mathematical model is essential for the control design as well as analysis of the PV system. In this section the mathematical model of the uncontrolled PV system is formulated. The overall model consists of three sets of equations which describe the PV matrix, the DC-link voltage dynamics and the AC-side current dynamics of the PV system. The model of the uncontrolled PV system along with those of the controllers constitute a model for the closed-loop PV system.

2.3.1 Space-Phasor Representation of the PV System

The PV matrix is described by the following equations [32]:

$$i_{pv} = n_p I_{ph} - n_p I_{rs}\left[\exp\left(\frac{q}{kT_cA}\frac{v_{dc}}{n_s}\right) - 1\right] \tag{2.1}$$

where q is the unit charge, k is Boltzman's constant, A is the p-n junction ideality factor, and T_c is the cell temperature. I_{rs} is the cell reverse saturation current, which varies with temperature according to the following equation:

$$I_{rs} = I_{rr}\left[\frac{T_c}{T_r}\right]^3 \exp\left(\frac{qE_G}{kA}\left[\frac{1}{T_r} - \frac{1}{T_c}\right]\right) \tag{2.2}$$

where T_r is the cell reference temperature, I_{rr} is the reverse saturation current at T_r, and E_G is the band-gap energy of the cell. The photovoltaic current, I_{ph}, depends on the insolation level and the cell temperature as:

$$I_{ph} = 0.01\,[I_{scr} + K_\vartheta\,(T_c - T_r)]\,S \tag{2.3}$$

where I_{scr} is the cell short-circuit current at the reference temperature and radiation, K_ϑ is a temperature coefficient, and S is the insolation level in kW/m^2. The

power delivered by the PV matrix is calculated by multiplying both the sides of (2.1) by v_{dc}:

$$P_{pv} = n_p I_{ph} v_{dc} - n_p I_{rs} v_{dc} \left[\exp\left(\frac{q}{kT_c A} \frac{v_{dc}}{n_s} \right) - 1 \right] \tag{2.4}$$

Based on (2.4), it is evident that the power delivered by the PV matrix is a function of I_{ph} which depends on the insolation level, S. Fig. 2.2 illustrates the power versus voltage characteristic of the PV matrix for different insolation levels. Fig. 2.2 shows that for a given insolation level, P_{pv} is zero at $v_{dc} = 0$, but increases as v_{dc} is increased. However, this trend continues only up to a certain value of v_{dc} at which P_{pv} peaks; beyond this point, P_{pv} decreases with the increase of v_{dc}. Thus, P_{pv} can be maximized by control of v_{dc}, based on a Maximum Power Point Tracking (MPPT) strategy [32].

In the PV system of Fig. 2.1, the VSC is a 6-pulse converter employing Insulated Gate Bipolar Transistor (IGBT) switches, adopting the Sinusoidal Pulse-Width Modulation (SPWM) strategy. The output voltage of the VSC, $\vec{v_t}$, is re-

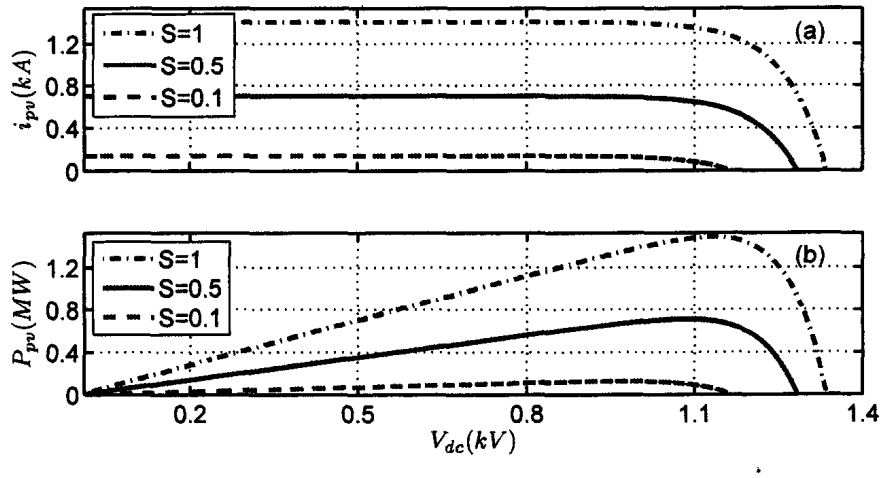

Figure 2.2: Current versus voltage and power versus voltage characteristics of a PV matrix

lated to v_{dc} as:

$$\vec{v_t} = \frac{v_{dc}\vec{m}}{2} \tag{2.5}$$

where $\vec{v_t}$ and $\vec{m}$ are the space-phasors, [33], corresponding to the VSC terminal voltages and the PWM modulating signals.

Dynamics of the DC-link voltage are governed by the principle of power balance, as [34]:

$$\frac{C}{2}\frac{dv_{dc}^2}{dt} = P_{pv} - P_{dc} \tag{2.6}$$

where P_{dc} denotes the power drawn by the VSC DC-side (see Fig. 2.1). Ignoring the VSC power loss, P_{dc} is assumed to be equal to P_t, i.e. the real power exiting the VSC AC-side terminals. P_t in turn is the summation of the real power delivered at the PCC, i.e. P_s, and the (real) power absorbed by the $R-L$ branch of the interface filter. Therefore,

$$\begin{aligned} P_{dc} &\approx P_t \\ &= \underbrace{\frac{3}{2}\mathrm{Re}\left\{\vec{v_s}\vec{i^*}\right\}}_{P_S} + \underbrace{\frac{3}{2}\mathrm{Re}\left\{R\vec{i}\,\vec{i^*}\right\}}_{P_R} + \underbrace{\frac{3}{2}\mathrm{Re}\left\{L\frac{d\vec{i}}{dt}\vec{i^*}\right\}}_{P_L} \end{aligned} \tag{2.7}$$

where $*$ denotes the complex-conjugate operator. Substituting for P_{dc} from (2.7) in (2.6), one finds

$$\frac{C}{2}\frac{dv_{dc}^2}{dt} = P_{pv} - \underbrace{\frac{3}{2}\mathrm{Re}\left\{\vec{v_s}\vec{i^*}\right\}}_{P_S} + \underbrace{\frac{3}{2}\mathrm{Re}\left\{R\vec{i}\,\vec{i^*}\right\}}_{P_R} + \underbrace{\frac{3}{2}\mathrm{Re}\left\{L\frac{d\vec{i}}{dt}\vec{i^*}\right\}}_{P_L}. \tag{2.8}$$

Equation (2.8) represents the dynamics of the DC-link voltage in a space-phasor form. The VSC AC-side current dynamics are described by the following space-phasor equation:

$$L\frac{d\vec{i}}{dt} = -R\vec{i} + \vec{v_t} - \vec{v_s} \tag{2.9}$$

Substituting for $\vec{v}_t$ from (2.5) in (2.9), one deduces:

$$L\frac{d\vec{i}}{dt} = -R\vec{i} + \frac{v_{dc}}{2}\vec{m} - \vec{v_s} \tag{2.10}$$

Equation (2.10) is used for the design of the VSC current controller.

2.3.2 DQ-Frame Representation of the PV system

For the purposes of analysis and control, the space-phasor variables of the PV system model are projected on a *dq*-frame. Transformation of the variables from the space-phasor form to the *dq*-frame form results in equivalent DC variables, which simplify the analysis and control design tasks. Moreover, a *dq*-frame-based control can be implemented more conveniently compared to the case where the control signals are time-varying. The transformation is defined as:

$$\vec{f} = (f_d + jf_q)e^{j\rho} \tag{2.11}$$

where $\vec{f}$ represents a space-phasor, f_d and f_q are the space-phasor *dq*-frame components, and ρ is the reference angle of the *dq*-frame. Another useful quantity is the derivative of a space-phasor, that is:

$$\begin{aligned}\frac{d\vec{f}}{dt} &= \frac{d\left[\left(f_d + jf_q\right)e^{j\rho}\right]}{dt} \\ &= \left(\frac{df_d}{dt} + j\frac{df_q}{dt}\right)e^{j\rho} + j\frac{d\rho}{dt}\left(f_d + jf_q\right)e^{j\rho} \\ &= \left(\frac{df_d}{dt} + j\frac{df_q}{dt}\right)e^{j\rho} + j\omega\left(f_d + jf_q\right)e^{j\rho}\end{aligned} \tag{2.12}$$

where ω is the *dq*-frame angular speed, as

$$\omega = \frac{d\rho}{dt}. \tag{2.13}$$

Based on (2.11), P_s in (2.7) can be expressed as:

$$P_s = \frac{3}{2}\mathrm{Re}\left\{\underbrace{\left[\left(v_{sd} + jv_{sq}\right)e^{j\rho}\right]}_{\vec{v}_s}\underbrace{\left[\left(i_d + ji_q\right)e^{-j\rho}\right]^*}_{\vec{i}^*}\right\}, \tag{2.14}$$

which can further be simplified to

$$P_s = \frac{3}{2}\left(v_{sd}i_d + v_{sq}i_q\right) \tag{2.15}$$

Similarly, the dq-frame equivalent of P_R in (2.7) is deduced as:

$$P_R = \frac{3}{2}R\left(i_d^2 + i_q^2\right) \tag{2.16}$$

In addition, based on (2.11) and (2.12), P_L in (2.7) is simplified to

$$P_L = \frac{3}{2}L\left(i_d\frac{di_d}{dt} + i_q\frac{di_q}{dt}\right) \tag{2.17}$$

Substituting in (2.8) for P_s, P_R, and P_L, respectively from (2.15), (2.16), and (2.17) one finds:

$$\frac{C}{2}\frac{dv_{dc}^2}{dt} = P_{pv} - \frac{3}{2}\left(v_{sd}i_d + v_{sq}i_q\right) - \frac{3}{2}R\left(i_d^2 + i_q^2\right) - \frac{3}{2}L\left(i_d\frac{di_d}{dt} + i_q\frac{di_q}{dt}\right). \tag{2.18}$$

Equation (2.18) is employed in designing a voltage regulator to maintain the DC-link voltage, v_{dc}, at a desired level, such that the power out of the PV matrix can be maximized.

A similar procedure as the one adopted to derive (2.18) yields the following dq-frame equivalents for (2.10):

$$L\frac{di_d}{dt} = L\omega i_q - Ri_d + m_d\frac{v_{dc}}{2} - v_{sd} \tag{2.19}$$

$$L\frac{di_q}{dt} = -L\omega i_d - Ri_q + m_q\frac{v_{dc}}{2} - v_{sq}. \tag{2.20}$$

Equations (2.18), (2.19), and (2.20) constitute a state-space model for the VSC, in which v_{dc}^2, i_d, i_q are the state variables, m_d and m_q are the control inputs, and v_{sd}, v_{sq}, and S are the exogenous inputs.

2.4 PV System Control

The main control task pertinent to the PV system of Fig. 2.1 is to regulate the DC-link voltage, to maximize the power extracted from the PV matrix. As shown in Fig. 2.1, the control involves the following three coordinated tasks:

- the VSC PWM and control schemes are synchronized to the PCC voltage through a Phase-Locked Loop (PLL) [35]. This ensures that the three-phase AC signals are transformed into dq-frame counterparts, and the controllers process the DC equivalents of the original sinusoidally-varying signals;

- the error between (the square of) the DC-link voltage, i.e. v_{dc}^2, and its corresponding reference value, v_{dcref}^2, is processed by a compensator, $k_v(s)$, whose output is augmented by a feed-forward signal to generate the current command i_{dref}. The feed-forward compensation counteracts the destabilizing, nonlinear, characteristic of the PV matrix and enhances the PV system stability. v_{dcref} is usually obtained from an MPPT scheme and is permitted to vary from a lower limit to an upper limit (not shown in Fig. 2.1), to ensure proper and safe operation of the VSC; and

- the command i_{dref} is delivered to a dq-frame, current-control scheme that forces i_d to track i_{dref}. The control of i_d enables the control of P_s and P_{pv}. i_{dref} is limited by a saturation block (not shown in Fig. 2.1) to protect the VSC against overload and faults. The current-control scheme also forces i_q to track i_{qref}. As discussed in Section 2.4.1, Q_s is proportional to i_q. Therefore, to ensure that the PV system exhibits a unity power-factor to the network, i_{qref} is set to zero, to make $Q_s = 0$. This also maintains the mag-

nitude of the VSC line current at a minimum, for a given real power flow. In subsequent sections, the foregoing three control schemes are discussed in detail.

2.4.1 Phase-Locked Loop (PLL)

As discussed in Section 2.3.2, the AC variables of the PV system are projected on a dq frame the rotational speed of which is ω. In a steady state, the AC variables are sinusoidal functions of the grid frequency ω_0. Thus, their dq-frame components become time-invariant (in the steady-state) if the dq–frame angular speed ω becomes equal to ω_0. This is achieved by means of a PLL mechanism [35]. A block diagram of the PLL adopted in this research is presented in Fig. 2.3. As Fig. 2.3 shows, $\vec{v_s}$ is resolved into its d– and q–axis components, based on (2.11). Then, v_{sq} is processed by the compensator $H(s)$, and ω is determined. In a steady state, v_{sq} is forced to zero while ω becomes equal to ω_0. Therefore, $H(s)$ must include at least one integrator.

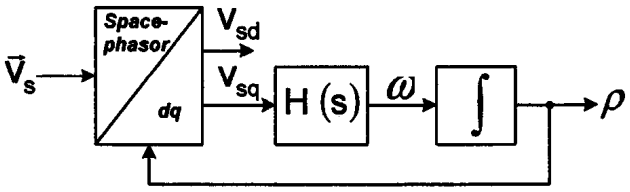

Figure 2.3: Block diagram of the Phase-Locked Loop (PLL)

Let $H(s)$ be a PI compensator cascaded with a first-order, low-pass, transfer-function, as

$$\begin{aligned}\Omega &= H(s)V_{sq} \\ &= \frac{\beta_1 s + \beta_2}{s(s+\beta_3)}V_{sq}\end{aligned} \tag{2.21}$$

where β_1 and β_2 are the proportional and integral gains of the PI part, respectively, whereas β_3 is the pole of the low-pass function of the compensator. Let the two state variables ξ_1 and ξ_2 are defined as

$$X_7 = \frac{V_{sq}}{s^2 + \beta_3 s} \tag{2.22}$$

$$X_6 = sX_2 \tag{2.23}$$

then, the PLL is described by the state-space model

$$\frac{d}{dt}X_{pll} = A_{pll}X_{pll} + B_{pll}\begin{bmatrix} v_{sd} \\ v_{sq} \end{bmatrix} \tag{2.24}$$

$$\omega = E_{pll}X_{pll} \tag{2.25}$$

$$\rho = F_{pll}X_{pll} \tag{2.26}$$

where

$$A_{pll} = \begin{bmatrix} -\beta_3 & 0 & 0 \\ 1 & 0 & 0 \\ \beta_1 & \beta_2 & 0 \end{bmatrix} \tag{2.27}$$

$$B_{pll} = \begin{bmatrix} 0 & 1 \\ 0 & 0 \\ 0 & 0 \end{bmatrix} \tag{2.28}$$

$$E_{pll} = \begin{bmatrix} \beta_1 & \beta_2 & 0 \end{bmatrix} \tag{2.29}$$

$$F_{pll} = \begin{bmatrix} 0 & 0 & 1 \end{bmatrix} \tag{2.30}$$

$$X_{pll} = \begin{bmatrix} x_6 & x_7 & \rho \end{bmatrix}^T. \tag{2.31}$$

Equations (2.24) through (2.26) introduce the PLL as a dynamic system whose inputs are v_{sd} and v_{sq}, the state variables are ξ_1, ξ_2, and ρ and the outputs are ω and ρ. Regulation of v_{sq} at zero also has the implication that the expression for the PV system real-power output, i.e. (2.15), is simplified to

$$P_s = \frac{3}{2} v_{sd} i_d. \tag{2.32}$$

Hence, P_s is proportional to, and can be controlled by, i_d. Similarly, the dq-frame expression for the reactive power assumes the form:

$$\begin{aligned} Q_s &= \frac{3}{2}\mathrm{Im}\left\{\vec{v}_s \vec{i}^*\right\} \\ &= \frac{3}{2}\mathrm{Im}\left\{\underbrace{\left[\left(v_{sd} + jv_{sq}\right)e^{j\rho}\right]}_{\vec{v}_s}\underbrace{\left[\left(i_d + ji_q\right)e^{-j\rho}\right]^*}_{\vec{i}^*}\right\} \\ &= \frac{3}{2}(v_{sq} i_{sd} - v_{sd} i_{sq}). \end{aligned} \tag{2.33}$$

which can be further simplified to:

$$Q_s = -\frac{3}{2} v_{sd} i_q. \tag{2.34}$$

Equation (2.34) indicates that Q_s can be controlled by i_q to adjust the power-factor that the PV system exhibits to the distribution network.

2.4.2 VSC Current Control

Equations (2.32) and (2.34) show the dependence of P_s and Q_s on i_d and i_q, respectively. In this section, a current-control scheme is presented to ensure that i_d and i_q rapidly track their respective reference commands, i_{dref} and i_{qref}. The current-control strategy also protects the VSC against overload and faults if i_{dref} and i_{qref} are limited. The current-control scheme is designed based on (2.19) and (2.20) which describe the dynamics of the VSC AC-side current. In (2.19) and (2.20), i_d and i_q are the state variables and also the outputs; m_d and m_q are the control inputs, and v_{sd}, v_{sq}, ω, and v_{dc} are the disturbances. Due to the presence of the factor $L\omega$, dynamics of i_d and i_q are coupled and nonlinear. To decouple and linearize the dynamics, m_d and m_q are determined based on the control laws [36]:

$$m_d = \frac{2}{v_{dc}} \left(u_d - L\omega i_q + v_{sd} \right) \tag{2.35}$$

$$m_q = \frac{2}{v_{dc}} \left(u_q + L\omega i_d + v_{sq} \right) \tag{2.36}$$

where u_d and u_q are two new control inputs. Substituting for m_d and m_q in (2.19) and (2.20), one obtains

$$L\frac{di_d}{dt} = -Ri_d + u_d \tag{2.37}$$

$$L\frac{di_q}{dt} = -Ri_q + u_q. \tag{2.38}$$

Equations (2.37) and (2.38) represent two decoupled, first-order, systems in which i_d and i_q can be controlled by u_d and u_q, respectively. Fig. 2.4 illustrates a block diagram of the dq-frame current-control scheme. Fig. 2.4 shows that the con-

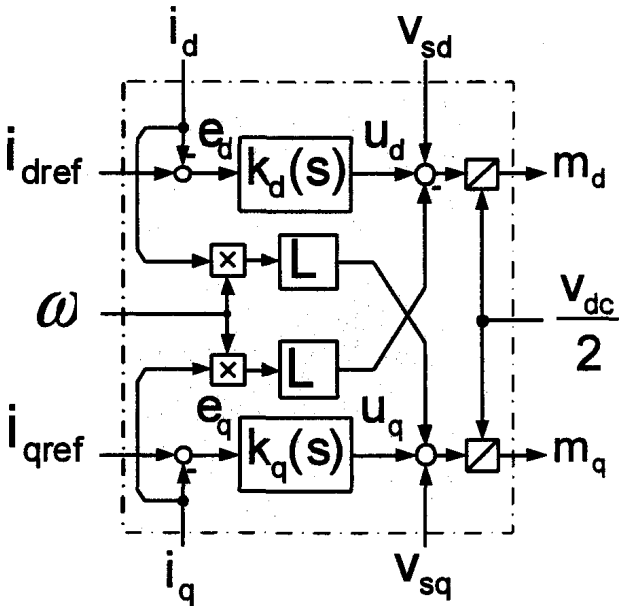

Figure 2.4: Block diagram of the dq-frame current control scheme

trol signal u_d is the output of a compensator, $k_d(s)$, processing the error signal $e_d = i_{dref} - i_d$. Similarly, u_q is the output of another compensator, $k_q(s)$, that processes $e_q = i_{qref} - i_q$. It should be noted that, to produce m_d and m_q, the signals $2/v_{dc}$, ωi_d, and ωi_q are employed as feed-forward terms to decouple the dynamics of i_d and i_q from that of v_{dc}.

The PWM modulating signals are generated by the transformation of m_d and

m_q into m_a, m_b and m_c, based on:

$$\begin{bmatrix} m_a \\ m_b \\ m_c \end{bmatrix} = \begin{bmatrix} \cos(\rho) & -sin(\rho) \\ \cos(\rho - \frac{2\pi}{3}) & -\sin(\rho - \frac{2\pi}{3}) \\ \cos(\rho - \frac{4\pi}{3}) & -\sin(\rho - \frac{4\pi}{3}) \end{bmatrix} \begin{bmatrix} m_d \\ m_q \end{bmatrix} \tag{2.39}$$

m_a, m_b, and m_c are then compared with a triangular PWM carrier signal, and the switching pulses are generated for the VSC valves.

Since the d- and q-axis control plants are identical, the compensators $k_d(s)$ and $k_q(s)$ can be picked to be identical. Let the compensator be of a PI type as:

$$k_d(s) = k_q(s) = \frac{k_p s + k_i}{s} \tag{2.40}$$

where k_p and k_i are the proportional and integral gains, respectively. If k_p and k_i are selected as

$$k_p = \frac{L}{\tau_i} \tag{2.41}$$

$$k_i = \frac{R}{\tau_i} \tag{2.42}$$

then, the closed-loop transfer-functions of the d- and q- axis current controllers assume the first-order form

$$\frac{I_d}{I_{dref}} = \frac{I_q}{I_{qref}} = G_i(s) = \frac{1}{\tau_i s + 1} \tag{2.43}$$

where τ_i is the time-constant, usually selected in the range of 0.5 to 5 ms, depending on the desired speed of response. It is noted that the foregoing control strategy renders the dynamic of i_d and i_q decoupled from those of ω, v_{dc}, v_{sd} and v_{sq}. Equation (2.43) can be expressed in a state-space form as:

$$\frac{d}{dt}\begin{bmatrix} i_d \\ i_q \end{bmatrix} = -\begin{bmatrix} \frac{1}{\tau_i} & 0 \\ 0 & \frac{1}{\tau_i} \end{bmatrix}\begin{bmatrix} i_d \\ i_q \end{bmatrix} + \begin{bmatrix} \frac{1}{\tau_i} & 0 \\ 0 & \frac{1}{\tau_i} \end{bmatrix}\begin{bmatrix} i_{dref} \\ i_{qref} \end{bmatrix}. \tag{2.44}$$

2.4.3 DC-Link Voltage Control and Feed-Forward Compensation

Equation (2.18) describes the dynamics of the DC-link voltage. In (2.18), the first and second terms represent the PV matrix power and the PV system real-power, respectively, whereas the third and fourth terms denote the power absorbed by the inductance and resistance of the VSC interface reactor. As discussed in Section 2.4.1, the PLL ensures that v_{sq} is regulated at zero. Therefore, if the power of the interface reactor is ignored, (2.18) can be approximated as:

$$\begin{aligned}\frac{C}{2}\frac{dv_{dc}^2}{dt} &\approx P_{pv} - \frac{3}{2}v_{sd}i_d \\ &\approx P_{pv} - \frac{3}{2}v_{sd}i_{dref}.\end{aligned} \tag{2.45}$$

Equation (2.45) represents a control plant of which the input is i_{dref}, the output is v_{dc}^2, and the disturbance input is v_{sd}. It should be noted that, in deducing (2.45), it is assumed that τ_i is small in (2.44) and therefore i_d can be substituted by i_{dref}.

Equation (2.45) indicates that the control of the DC-link voltage is a nonlinear process. The reasons is mainly that P_{pv} is a nonlinear function of v_{dc} and i_{pv}. Thus, to mitigate the impact of the nonlinearity on the control, i_{dref} is determined based on the following control law:

$$i_{dref} = u_v + \gamma \underbrace{\frac{P_{pv}}{\frac{3}{2}v_{sd}}}_{i_{ff}} \tag{2.46}$$

where u_v is a new control input and $i_{ff} = P_{pv}/(\frac{3}{2}v_{sd})$ is a feed-forward term with γ as a gain which can be unity or zero. γ as a gain which can be unity or zero. Substituting for i_{dref} from (2.46) in (2.45), one deduces:

$$\frac{C}{2}\frac{dv_{dc}^2}{dt} \approx (1-\gamma)P_{pv} - \frac{3}{2}v_{sd}u_v \tag{2.47}$$

Equation (2.47) indicates that if $\gamma = 1$, the impact of the PV matrix characteristic on the DC-link voltage control is eliminated, and the effective control plant becomes an integrator. Thus, the feed-forward compensation effectively counteracts the dynamics of P_{pv} and prevents them from manifesting themselves in (2.47). The end result is that v_{dc} is controlled predominantly by the control variable u_v. Even though the product $v_{sd}u_v$ also introduces a nonlinearity, its impact is insignificant since v_{sd} is practically a relatively constant variable.

The control signal u_v is determined by a compensator as

$$U_v = k_v(s)E_v = \frac{\alpha_1 s + \alpha_2}{s(s+\alpha_3)}E_v \tag{2.48}$$

where the error signal is $E_v = \pounds\{v_{dcref}^2 - v_{dc}^2\}$. Equation (2.48) represents a PI compensator cascaded with a first-order, low-pass, filter. α_1 and α_2 are the proportional and integral gains of the PI part of the compensator, respectively, whereas α_3 is the pole of the low-pass function.

Fig. 2.5 illustrates a block diagram of the DC-link voltage control scheme. As Fig. 2.5 indicates, if $\gamma = 1$ the impact of P_{pv} does not manifest itself in i_d. On the other hand, i_d is related to u_v through i_{dref} and the transfer function (2.43). Consequently, the effective control plant from u_v to v_{dc}^2 is composed of an integrator cascaded with $G_i(s)$. Substituting for u_v from (2.48) in (2.46), one obtains an expression for i_{dref} with the feed-forward compensation, as:

$$i_{dref} = \pounds^{-1}\left\{\frac{\alpha_1 s + \alpha_2}{s(s+\alpha_3)}\right\} \star \left\{v_{dcref}^2 - v_{dc}^2\right\} + \gamma\frac{P_{pv}}{\frac{3}{2}v_{sd}} \tag{2.49}$$

If the two state variables x_3 and x_4 are defined as

$$X_3 = \frac{\pounds\{v_{dcref}^2 - v_{dc}^2\}}{s(s+\alpha_3)} \tag{2.50}$$

$$X_4 = sX_3 \tag{2.51}$$

then, the state-space model of DC-link voltage controller is expressed as:

$$\frac{d}{dt}\begin{bmatrix} x_3 \\ x_4 \end{bmatrix} = \begin{bmatrix} 0 & 1 \\ 0 & -\alpha_3 \end{bmatrix}\begin{bmatrix} x_3 \\ x_4 \end{bmatrix} + \begin{bmatrix} 0 \\ -1 \end{bmatrix} v_{dc}^2 + \begin{bmatrix} 0 \\ 1 \end{bmatrix} v_{dcref}^2 \tag{2.52}$$

$$i_{dref} = \begin{bmatrix} \alpha_2 & \alpha_1 \end{bmatrix}\begin{bmatrix} x_3 \\ x_4 \end{bmatrix} + \gamma \frac{P_{pv}}{\frac{3}{2}v_{sd}} \tag{2.53}$$

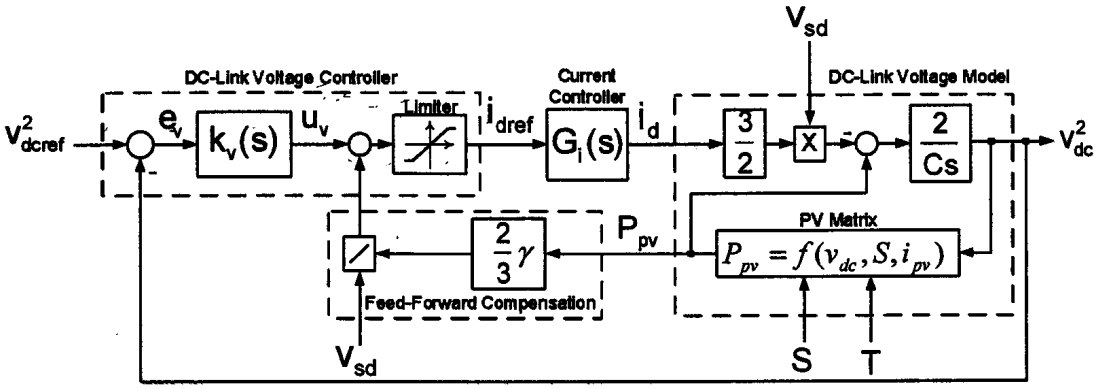

Figure 2.5: Block diagram of the voltage control scheme

2.5 Model Validation

In this section, simulation studies are conducted on a detailed switched model of the PV system of Fig. 2.1. The simulations are conducted in the PSCAD/EMTDC software environment. The PV system of Fig. 2.1 simulated to

- evaluate the performance of the PV system under the proposed control strategy, and
- demonstrate the effectiveness of the feed-forward compensation of the DC-link voltage controller

2.5.1 Case 1

This case study demonstrates the performance of the PV system of Fig. 2.1 and the feed-forward scheme. Fig. 2.6 shows the response of v_{dc} and i_d for different insolation levels when v_{dcref} is changed step-wise from 1.0 kV to 1.1 kV. Columns (a) and (b), respectively, demonstrate the responses of v_{dc} and i_d. It can be observed that, the DC-link voltage controller tracks the value set by v_{dcref} in less than 10 ms. Moreover, the change in v_{dc} results in a change in i_d, which translates into a proportional change in the output real power of the PV system (based on (2.32)). It is interesting to note that the increase of v_{dc} results in the increase of the output power, except for the case $S = 0.1$. The reason is that for $S = 0.1$, the DC-link voltage corresponding to the maximum power is about 1.0 kV. Consequently, any increase of v_{dc} beyond 1.0 kV results in an output power drop.

2.5.2 Case 2

Fig. 2.7(a) shows that, initially, $v_{dc} = 1\ kV$ (at $S = 1$), and the current of the PV matrix, i_{pv}, is 1.4 kA as shown in Fig. 2.7(b). The feed-forward compensation is enabled. As shown in Fig. 2.7(c), the d-axis component of VSC AC-side current, i_d, is about 2.25 kA, which correspond to an (real) output power of about 1.34 MW, as illustrated in Fig. 2.7(d). At $t = 2.0\ s$, v_{dcref} is changed stepwise to 1.22 kV. Consequently, v_{dc} tracks v_{dcref} in less than 10 ms, as shown in Fig. 2.7(a). Fig. 2.7(b) illustrates that i_{pv} drops from 1.4 kA to 1.1 kA, in response to the step change in v_{dc}. Figs. 2.7(c) and (d) show that i_d and P_s settle at the values 2.25 kA and 1.34 MW, respectively. At $t = 2.4\ s$, v_{dcref} is changed stepwise from 1.22 kV

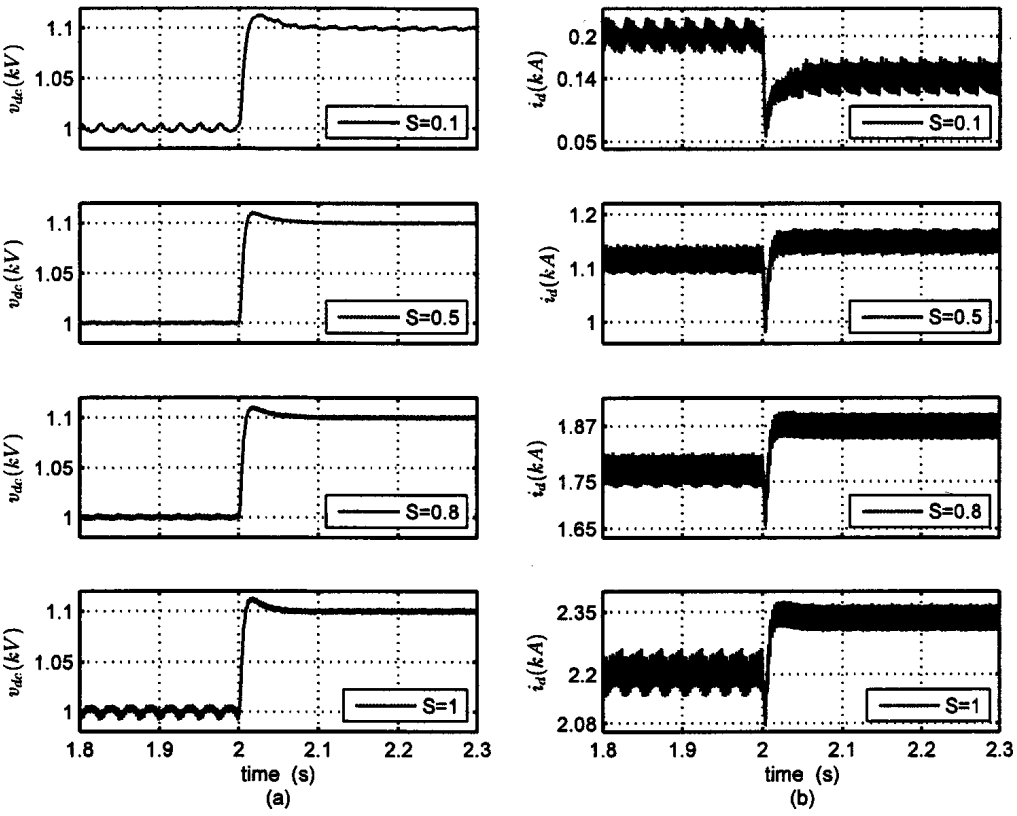

Figure 2.6: Response of v_{dc} and i_d at different insolation levels when a 10% step change is imposed on v_{dcref}

to 1.0 kV. At $t = 2.5$ s, the feed-forward compensation is disabled. Consequently the PV system becomes oscillatory thereafter, as Fig. 2.7 shows. This case study confirms the effectiveness of the feed-forward compensation, and that without the feed-forward compensation, the stability of the PV system is dependent on the operating point.

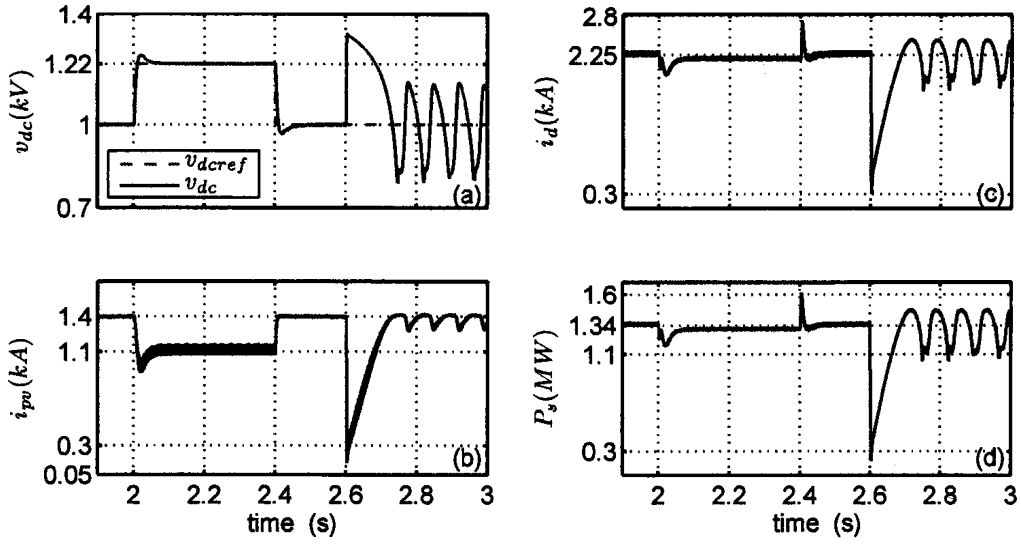

Figure 2.7: Transient behaviors of P_s, i_{pv}, and i_d in response to step changes in v_{dcref}, and de-activation of the feed-forward compensation in the DC-link voltage controller

2.6 Conclusion

In this chapter, a mathematical model is developed for a PhotoVoltaic system that is interfaced with a stiff grid. Based on the developed model, a control methodology is identified for the PV system. The proposed control strategy is based on an inner current-control scheme and an outer DC-link voltage control scheme. Proper feed-forward compensation strategies are adopted to make the current-control scheme independent of the rest of the system. Further, a feed-forward compensation mechanism is also proposed for the DC-link voltage control loop to mitigate the impact of nonlinearity of the PV panels on the control of the PV system. The developed model is validated through case studies in the PSCAD/EMTDC software environment, and the effectiveness of the proposed feed-forward control strategy is confirmed.

Chapter 3

Performance of a PhotoVoltaic (PV) System Interfaced with a Distribution Network

3.1 Introduction

In chapter 2, a mathematical model of a single-stage, three-phase, PV system was developed. The model developed in Chapter 2 was that of a PV system interfaced with a stiff grid. The model enabled the control design and optimization tasks, independently of the grid model. This chapter augments the model of Chapter 2 with those of the distribution network, and the loads. Then the overall model is used to identify some important transients of the overall system. The overall model will also be used in Chapter 4 for stability analysis and the assessment of the interactions between the PV system and the network.

3.2 Description of the Model

Consider the PV system of Fig. 2.1. Fig. 3.1 shows that the PV system is interfaced with a distribution network at a Point of Common Coupling (PCC). The distribution network is supplied from a stiff grid which is represented by a voltage source v_g. A squirrel-cage asynchronous machine, employed here as a load, is connected to the distribution line at a location between the PCC and the grid. The inductance and resistance of the line segment between the PCC and the load are represented by L_1 and R_1, respectively. L_2 and R_2, respectively, signify the inductance and resistance of the line segment between the load and the grid. It should be noted that L_1 and R_1 also include the leakage and winding resistance of transformer T_{r1}, respectively. The capacitor C_l represents the load power-factor correction capacitor. However, for the purpose of analysis, C_l is considered as a component of the distribution network. P_s and Q_s, respectively, represent the real- and reactive-power components that the PV system exchanges with the distribution network, at the PCC.

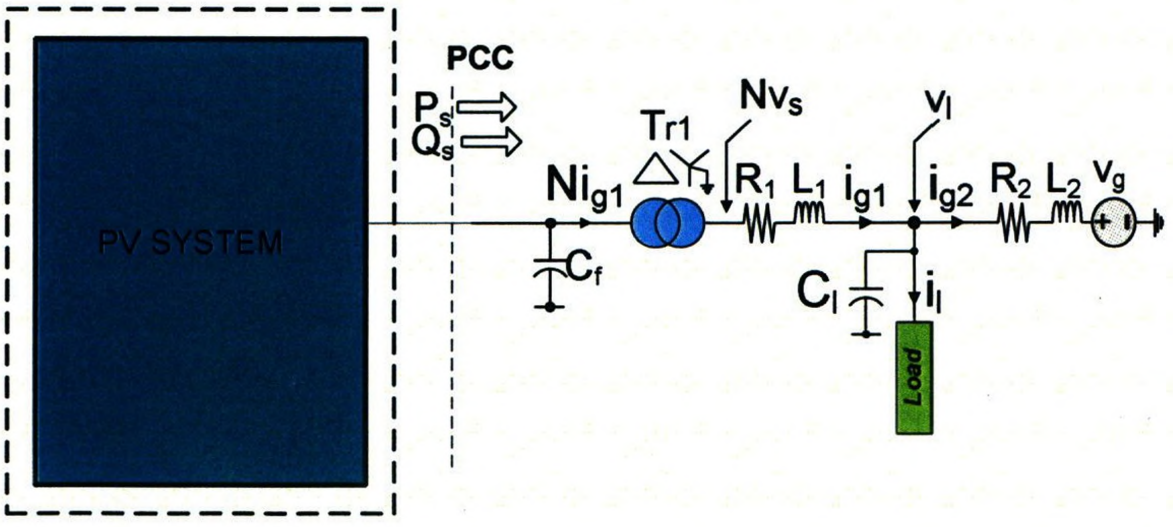

Figure 3.1: Schematic diagram of the PV system interfaced with a distribution network

3.3 Distribution Network Model

The dynamics of distribution network in the space-phasor form can be explained by the following sets of equations:

$$L_1 \frac{d\vec{i}_{g1}}{dt} = -R_1 \vec{i}_{g1} - \vec{v}_l + \vec{v}_s \tag{3.1}$$

$$L_2 \frac{d\vec{i}_{g2}}{dt} = -R_2 \vec{i}_{g2} - \vec{v}_g + \vec{v}_l \tag{3.2}$$

$$C_f \frac{d\vec{v}_s}{dt} = \vec{i} - \vec{i}_{g1} \tag{3.3}$$

$$C_l \frac{d\vec{v}_l}{dt} = \vec{i}_{g1} - \vec{i}_{g2} - \vec{i}_l \tag{3.4}$$

As discussed in Section 2.4, the controllers of the PV system are designed based on the *dq*-frame mathematical model. In order to study the behavior of the PV system in association with the distribution network, the equations describing the dynamics of the distribution network must be expressed in *dq*-frame equivalents. Hence, based on (2.11) and (2.12), the *dq*-frame equivalents of (3.1) through (3.4) are expressed as:

$$\frac{di_{g1d}}{dt} = -\frac{R_1}{L_1} i_{g1d} + \omega i_{g1q} + \frac{N}{L_1} v_{sd} - \frac{1}{L_1} v_{ld} \tag{3.5}$$

$$\frac{di_{g1q}}{dt} = -\omega i_{g1d} - \frac{R_1}{L_1} i_{g1q} + \frac{N}{L_1} v_{sq} - \frac{1}{L_1} v_{lq} \tag{3.6}$$

$$\frac{di_{g2d}}{dt} = -\frac{R_2}{L_2} i_{g2d} + \omega i_{g2q} + \frac{1}{L_2} v_{ld} - \frac{1}{L_2} \hat{v}_g \cos\theta \tag{3.7}$$

$$\frac{di_{g2q}}{dt} = -\omega i_{g2d} - \frac{R_2}{L_2} i_{g2q} + \frac{1}{L_2}\tilde{v}_{lq} + \frac{1}{L_2}\hat{v}_g \sin\theta \tag{3.8}$$

$$\frac{dv_{sd}}{dt} = \frac{1}{c_f} i_d - \frac{N}{c_f} i_{g1d} + \omega v_{sq} \tag{3.9}$$

$$\frac{dv_{sq}}{dt} = \frac{1}{c_f} i_q - \frac{N}{c_f} i_{g1q} - \omega v_{sd} \tag{3.10}$$

$$\frac{dv_{ld}}{dt} = \frac{1}{c_l} i_{g1d} - \frac{1}{c_l} i_{g2d} + \omega v_{lq} - \frac{1}{c_l} i_{ld} \tag{3.11}$$

$$\frac{dv_{lq}}{dt} = \frac{1}{c_l} i_{g1q} - \frac{1}{c_l} i_{g2q} - \omega v_{ld} - \frac{1}{c_l} i_{lq} \tag{3.12}$$

Equations (3.5) through (3.12) describe the dynamics of the distribution network in the dq-frame with i_{g1d}, i_{g1q}, i_{g2d}, and i_{g2q}, as state variables, and v_{sd}, v_{sq}, v_{ld}, and v_{lq} as the state variables as well as the outputs. The PV system AC-side current components, i_d and i_q, and the load current components, i_{ld} and i_{lq}, act as exogenous inputs for the distribution network.

3.4 Load Model

As discussed in Section 3.2, the asynchronous machine load, is connected to the distribution line at a point between the PCC and the grid. To measure the relative distance of the load with respect to the PV system, the factor d_f is introduced. Thus, d_f of value 0.5 corresponds to the case where the load is located in the middle of the PCC and the grid.

A space-phasor model of a squirrel-cage asynchronous machine is [37]

$$\frac{d\vec{\lambda}_s}{dt} = \vec{v}_l - R_s \vec{i}_s \tag{3.13}$$

$$\frac{d\vec{\lambda}_r}{dt} = -R_r \vec{i}_r \tag{3.14}$$

where R_s and R_r represent the stator and rotor resistances, respectively. $\vec{\lambda_s}$ and $\vec{\lambda_r}$ represent the space phasors corresponding to the stator and rotor flux linkages, respectively. Ignoring the magnetic saturation, one can write

$$\vec{\lambda_s} = L_m\left[(1+\sigma_s)\vec{i_s} + e^{j\theta_r}\vec{i_r}\right] \tag{3.15}$$

$$\vec{\lambda_r} = L_m\left[(1+\sigma_r)\vec{i_r} + e^{-j\theta_r}\vec{i_s}\right] \tag{3.16}$$

where L_m is the magnetizing inductance, and θ_r is the rotor angle. σ_s, σ_r, $\vec{i_s}$, and $\vec{i_r}$ denote the stator leakage factor, the rotor leakage factor, the stator current space-phasor, and the rotor current space-phasor, respectively. The machine electrical torque is formulated as

$$T_e = \frac{3}{2}L_m \mathrm{Im}\left\{\vec{i_s}\left(\vec{i_r}e^{j\theta_r}\right)^*\right\}. \tag{3.17}$$

The machine equations can be transformed into a state-space representation if the following changes of variables are introduced:

$$\vec{i_1} = (1+\sigma_s)\vec{i_s} + e^{j\theta_r}\vec{i_r} \tag{3.18}$$

$$\vec{i_2} = (1+\sigma_r)e^{j\theta_r}\vec{i_r} + \vec{i_s}. \tag{3.19}$$

Expressing $\vec{i_s}$ and $\vec{i_r}$ in terms of $\vec{i_1}$ and $\vec{i_2}$, based on (3.18) and (3.19), and substituting for them in (3.13) to (3.17), one deduces

$$L_m\frac{d\vec{i_1}}{dt} = \vec{v_l} - \frac{(1+\sigma_r)}{(1+\sigma_r)(1+\sigma_s)-1}R_s\vec{i_1} + \frac{1}{(1+\sigma_r)(1+\sigma_s)-1}R_s\vec{i_2} \tag{3.20}$$

$$\begin{aligned} L_m\frac{d\vec{i_2}}{dt} = {} & jL_m\omega_r\vec{i_2} + \frac{1}{(1+\sigma_r)(1+\sigma_s)-1}R_r\vec{i_1} \\ & -\frac{(1+\sigma_s)}{(1+\sigma_r)(1+\sigma_s)-1}R_r\vec{i_2} \end{aligned} \tag{3.21}$$

Moreover, the expression for the machine toque assumes the form:

$$T_e = \frac{3}{2} L_m \mathrm{Im}\left\{\overrightarrow{i_1}\,\overrightarrow{i_2}^*\right\}. \tag{3.22}$$

Assuming a two-mass representation of the mechanical system, one can write

$$J_r \frac{d\omega_r}{dt} = -D_r\omega_r - K_s(\theta_r - \theta_m) + \underbrace{\frac{3}{2} L_m \mathrm{Im}\left\{\overrightarrow{i_1}\,\overrightarrow{i_2}^*\right\}}_{T_e} \tag{3.23}$$

$$J_m \frac{d\omega_m}{dt} = -D_m\omega_m + K_s(\theta_r - \theta_m) - T_m \tag{3.24}$$

$$\frac{d\theta_r}{dt} = \omega_r \tag{3.25}$$

$$\frac{d\theta_m}{dt} = \omega_m \tag{3.26}$$

where J_r (J_m) is the machine (mechanical load) moment of inertia, ω_r (ω_m) is the machine (mechanical load) angular speed, θ_r (θ_m) is the machine (mechanical load) rotor angle, and D_r (D_m) is the machine (mechanical load) damping coefficient. K_s is the drive-train spring constant, and T_m is the mechanical load torque.

Equations (3.20), (3.21), and (3.23)-(3.26) constitute a state-space model for load subsystem. It should be noted that if T_m is set to a negative value, the asynchronous machine acts as a generator rather than a load. For example, an asynchronous generator can represent a constant-speed wind turbine-generator unit interfaced with the distribution network. dq-frame equivalents of state-space model of the asynchronous machine are:

$$\begin{aligned}\frac{di_{1d}}{dt} = &-\frac{(1+\sigma_r)}{(1+\sigma_r)(1+\sigma_s)-1}\frac{R_s}{L_m} i_{1d} + \omega i_{1q} \\ &+\frac{1}{(1+\sigma_r)(1+\sigma_s)-1}\frac{R_r}{L_m} i_{2d} + \frac{1}{L_m} v_{1d}\end{aligned} \tag{3.27}$$

$$\frac{di_{1q}}{dt} = -\omega i_{1d} - \frac{(1+\sigma_r)}{(1+\sigma_r)(1+\sigma_s)-1}\frac{R_s}{L_m}i_{1q} + \frac{1}{(1+\sigma_r)(1+\sigma_s)-1}\frac{R_r}{L_m}i_{2q} + \frac{1}{L_m}v_{lq} \tag{3.28}$$

$$\frac{di_{2d}}{dt} = \frac{1}{(1+\sigma_r)(1+\sigma_s)-1}\frac{R_r}{L_m}i_{1d} - \frac{(1+\sigma_s)}{(1+\sigma_r)(1+\sigma_s)-1}\frac{R_r}{L_m}i_{2d} + (\omega-\omega_r)\,i_{2q} \tag{3.29}$$

$$\frac{di_{2q}}{dt} = \frac{1}{(1+\sigma_r)(1+\sigma_s)-1}\frac{R_r}{L_m}i_{1q} - \frac{(1+\sigma_s)}{(1+\sigma_r)(1+\sigma_s)-1}\frac{R_r}{L_m}i_{2q} - (\omega-\omega_r)\,i_{2d} \tag{3.30}$$

$$\frac{d\omega_r}{dt} = -\frac{3L_m i_{1q}}{2J\left[(1+\sigma_r)(1+\sigma_s)-1\right]}i_{2d} - \frac{3L_m i_{1d}}{2J\left[(1+\sigma_r)(1+\sigma_s)-1\right]}i_{2q} - \frac{D}{J}\omega_r - \frac{1}{J}T_m \tag{3.31}$$

The load current, i.e the stator current, $\vec{i_s}$, is expressed in terms of $\vec{i_1}$ and $\vec{i_2}$ as

$$\vec{i_l} = \frac{(1+\sigma_r)}{(1+\sigma_r)(1+\sigma_s)-1}\vec{i_1} - \frac{1}{(1+\sigma_r)(1+\sigma_s)-1}\vec{i_2}. \tag{3.32}$$

$\vec{i_l}$ can then be expressed in the dq-frame as:

$$i_{ld} = \frac{(1+\sigma_r)}{(1+\sigma_r)(1+\sigma_s)-1}i_{1d} - \frac{1}{(1+\sigma_r)(1+\sigma_s)-1}i_{2d} \tag{3.33}$$

$$i_{lq} = \frac{(1+\sigma_r)}{(1+\sigma_r)(1+\sigma_s)-1}i_{1q} - \frac{1}{(1+\sigma_r)(1+\sigma_s)-1}i_{2q} \tag{3.34}$$

Equations (3.27)-(3.31) and (3.33)-(3.34) constitute the state-space model of the distribution network, in dq-frame. i_{1d}, i_{1q}, i_{2d}, and i_{2q}, are the state variables, and i_{ld} and i_{lq} are the outputs of the load subsystem.

3.5 PV System Transients

To evaluate the dynamic behavior of the PV system, in conjunction with the distribution network, the PV system of Fig.3.1 is simulated using a detailed switched model of the overall system. The simulation studies are conducted in the PSCAD/EMTDC environment to evaluate:

- the start-up transient of the PV system;
- the performance of the DC-link voltage regulation scheme under normal and faulty conditions;
- the ability of the PV system in operating at unity power factor and introducing a low level of harmonic currents to the distribution network;
- the robustness of the PV system against faults; and
- the need for and the effectiveness of the feed-forward compensation scheme in maintaining the stability of the PV system.

The system parameters are presented in Appendix A.

3.5.1 PV System Start-Up and Normal Operation

Fig. B.4 shows the system response to the start-up process followed by a steady-state condition. Initially, the system is connected to the distribution network while the PV system is disabled for a period of 0.2 s. The DC-link capacitor, C, is therefore pre-charged via anti-parallel diodes of the VSC valves, and v_{dc} reaches about 1.34 kV as shown in Fig. B.4(a). At t = 0.2 s, the VSC and controllers are activated. Consequently, v_{dc} smoothly settles at 1.0 kV set by v_{dcref},

and the PV matrix current, i.e. i_{pv}, rises to about 1.4 kA, as illustrated in Figs. B.4(a) and B.4(b), respectively. The rise in i_{pv} results in a sharp rise in i_d through the feed-forward mechanism of the DC-link voltage controller of the PV system, as shown in Fig. B.4(c). Fig. B.4(d) shows that P_s, i.e. power that the PV system real-power output increases from zero to about 1.36 MW, subsequent to the system start-up transient.

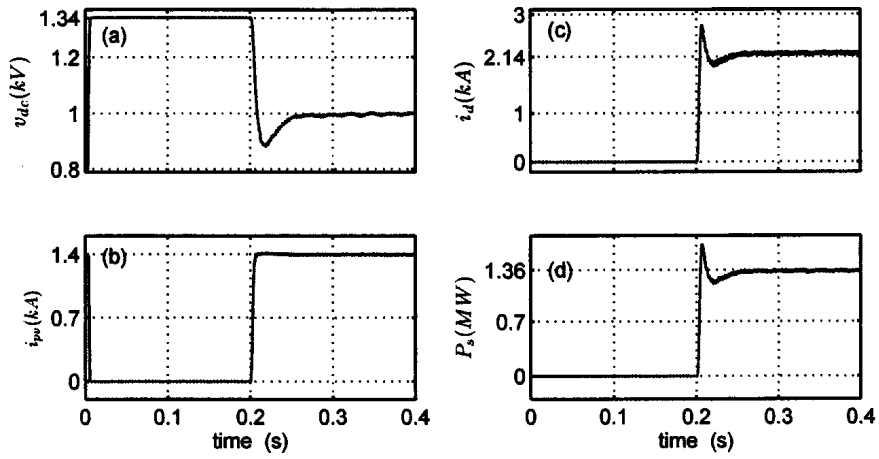

Figure 3.2: PV system transient response during the start-up process

Fig. 3.3(a) illustrates the effectiveness of the Phase-Locked Loop (PLL) mechanism in synchronizing the dq-frame to the PCC voltage. As Fig. 3.3(a) shows, subsequent to the start-up, v_{sd} and v_{sq} stabilize and v_{sq} settles at zero in less than 0.2 s. Thus, v_{sd} settles at a value of about 0.4 kV, i.e. the peak value of the PCC line-to-neutral voltage. Fig. 3.3(b) and 3.3(c), respectively illustrate the waveforms of i_q and Q_s, during the start-up process, and that they are both regulated at zero, irrespective of the transient and steady-state excursions of i_d and P_s, Fig. B.4. This confirms that the d and q-axis current controllers are decoupled.

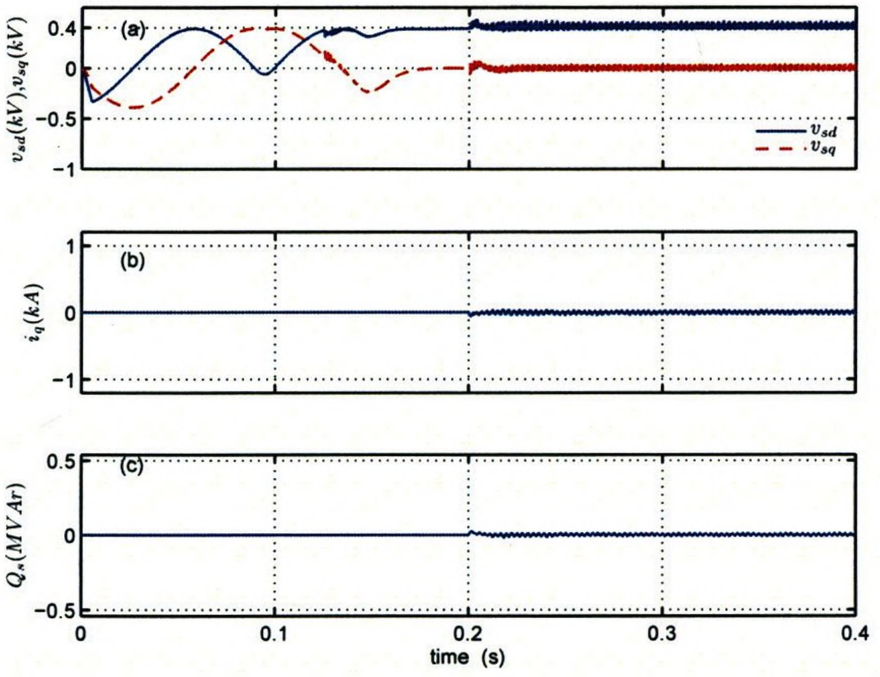

Figure 3.3: Synchronization and the responses of v_s, i_q, and Q_s during the start-up process

3.5.2 DC-Link Voltage Control and MPPT

As discussed in Section 2.3, the power of the PV matrix and, thus, the output (real) power of the PV system are highly dependent on the insolation and DC-link voltage levels. The following case study is to demonstrate the mechanism of and the need for a Maximum Power Point Tracking (MPPT) strategy.

Fig. 3.4(a) shows that the initial value of the insolation level is S =1 for this case study. This, at the DC-link voltage of 1.3 kV, Fig. 3.4(b), translates into an output power of 750 kW, as Fig. 3.4(c) indicates. For S = 1, the DC-link voltage v_{dc} = 1.3 kV is however different than the value corresponding to the maximum output power. At t = 2.0 s, v_{dc} is changed to 1.22 kV, Fig. 3.4(b), resulting in an increase of the output power to about 1.3 MW, as shown in 3.4(c). At t = 2.2 s, the insolation level changes stepwise to S = 0.8 while the DC-

link voltage reference is kept unchanged at $v_{dcref} = 1.22\ kV$. Consequently, the output power drops and settles at about 1.0 MW, Fig. 3.4(c). The output power is maximized for $S = 0.8$ when the DC-link voltage is reduced to 1.15 kV, at $t = 2.4\ s$. The optimum DC-link voltage of 1.15 kV corresponds to an output power of 1.13 MW, as Fig. 3.4(c) illustrates. This case study clearly illustrates how the output power can be significantly controlled (optimized) if the DC-link voltage is controlled over only a narrow range.

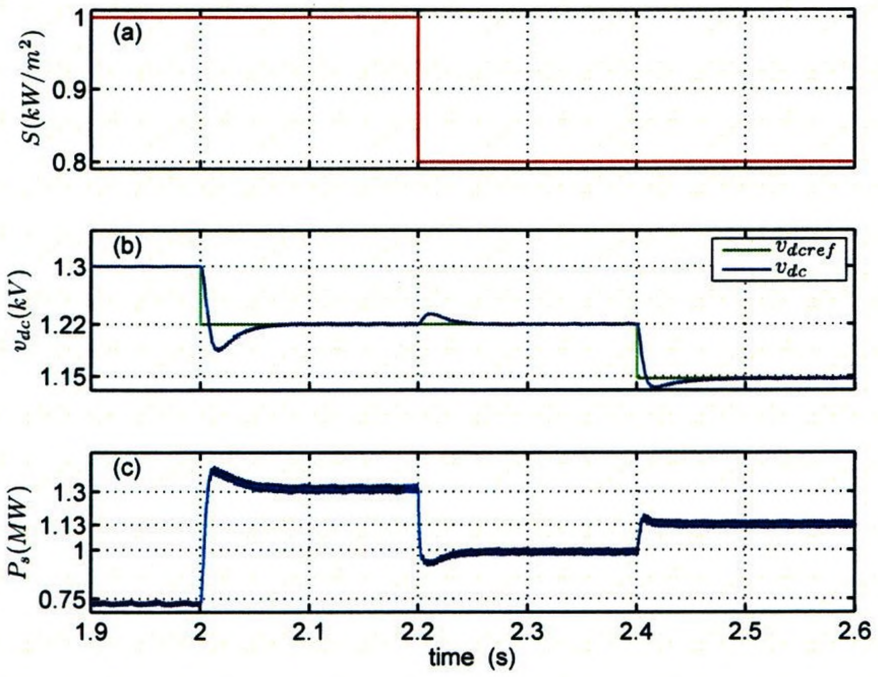

Figure 3.4: Control of P_s by means of DC-link voltage control

3.5.3 Independent Control of Real and Reactive Power

This case study is to demonstrate the capability of the PV system to independently control its real- and reactive-power output. For this case study, $S = 1$. Thus, as Fig. 3.5(a) shows, $v_{dc} = 1.32\ kV$ results in a real-power output of about 500 kW, Fig. 3.5(b). However, i_{qref} is set to zero and therefore Q_s is also zero as illustrated

in Fig. 3.5(b). Hence, the PCC phase voltage and the corresponding VSC line current are cophasal, Fig. 3.5(c). At t = 2.0 s, v_{dcref} is changed stepwise to 1.13 kV. Consequently, v_{dc} also reduces to and settles at 1.13 kV, Fig. 3.5(a) and P_s rises to about 1.5 MW. However, Q_s remains unchanged, as shown in Fig. 3.5(b). The increase in P_s results in a corresponding increase in the line current amplitude; however, the line current phase relative to the PCC voltage remains zero, as shown in Fig. 3.5(c).

At t =2.1 s, Q_s is changed to about 500 $kVAr$ while v_{dcref} is kept constant at 1.13 kV. Therefore, the line current rapidly lags the PCC voltage and its amplitude slightly increases, Fig. 3.5(c). The change in Q_s, however, does not impact P_s as shown in Fig. 3.5(b). At t = 2.15 s, Q_s is brought back to zero and the PV system again exhibits a unity power-factor to the distribution network.

It is interesting to note that the changes of Q_s momentarily disturb v_{dc} whereas they do not affect P_s. The reason is that a change of Q_s results in a corresponding change in the amplitude of the VSC line current which, in turn, results in a transient exchange of power with the line reactor of the VSC. Thus, the reactor absorbs power when the current amplitude increases, and vice-versa. However, since P_s is regulated and does not change, the transient reactor power must be necessarily exchanged with the VSC DC-side and DC-link capacitor. Consequently, v_{dc} gets disturbed.

3.5.4 Line-to-Ground Fault

To demonstrate the robustness of the PV system against external fault, a case study has been investigated in which phase (c) of the high-voltage side of T_{r1} is bolted to the ground for a duration of about three 60-Hz cycles. Fig. 3.6

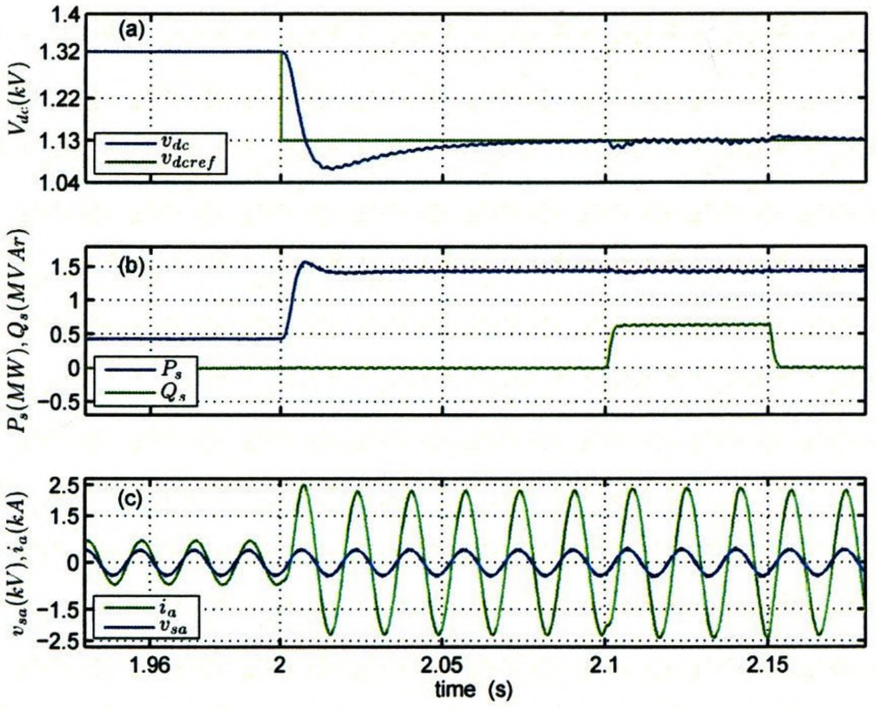

Figure 3.5: Transient behaviors of P_s and Q_s in response to step changes in i_{qref} and v_{dcref}

demonstrates the PV system response to the fault. During the fault, the voltage of faulted phase becomes zero, as Fig. 3.6(a) shows, and the line current becomes unbalanced and distorted, as illustrated in Fig. 3.6(b). This also results in fluctuations in P_s as well as a drop in its average value, Fig. 3.6(c). The fluctuations of P_s translate into fluctuations of v_{dc}, as shown in Fig. 3.6(d). Fig. 3.6 shows that, despite the severity of the fault, however, the PV system remains stable and retrieves its normal operation, subsequent to the fault clearance.

3.5.5 Performance without Feed-Forward Compensation

The cases discussed thus far assess the performance of the PV system when the feed-forward compensation of the DC-link voltage controller is enabled. The case studies illustrate that, employing the proposed control approach, the PV

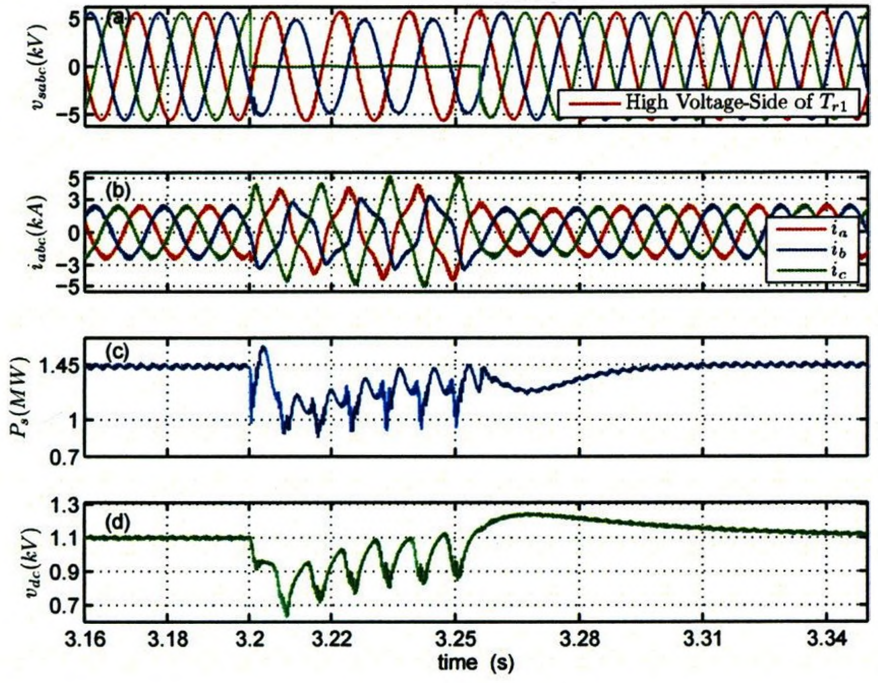

Figure 3.6: PV system response to a line-to-ground fault

system remains stable under various adverse conditions. However, this section demonstrates the performance of the PV system when the feed-forward compensation is disabled. It is shown in this section that, in the absence of the feed-forward compensation the PV system performance highly depends on its operating point, which is a property of a nonlinear system such as the PV system

Fig. 3.7(a) illustrates the start-up response of the PV system when v_{dcref} is set to 1.0 kV and the feed-forward control is disabled. It can be observed that v_{dc} approaches 1.0 kV, but oscillates with a frequency of about 15.6 Hz. A comparison between Fig. 3.7(a) and Fig. B.4(a) clearly confirms the difference between the cases with and without feed-forward compensation. Fig. 3.7(b) shows that the oscillations stop when v_{dcref} is changed from 1.0 kV to 1.1 kV, that is in the absence of feed-forward compensation, the system dynamics depend on the operating point.

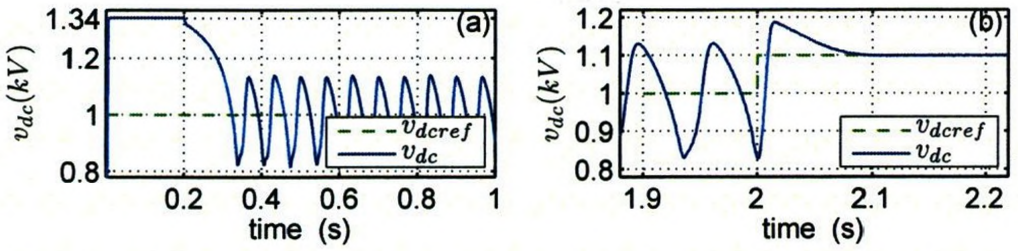

Figure 3.7: Response of DC-link voltage when feed-forward of the DC-link voltage controller is disabled

In this case study, to find the DC-link voltage at which the oscillations commence, v_{dcref} is gradually decreased towards lower values. Figs. 3.8(a) through (c) show that, down to 1.02 kV the PV system remains stable and damped. However, the damping becomes poorer as the DC-link voltage is reduced. Fig. 3.8(d) shows that the damping becomes zero and oscillations develop once v_{dcref} reaches a value of about 1.015 kV. The sustained oscillations result in similar oscillations in the output power, the PCC voltage, and the operating frequency of the PV system, as shown in Figs. 3.9(a) through (c). The oscillations penetrate into the distribution network and may excite the torsional mode of some motor loads of other consumers, as shown in Fig. 3.9(d).

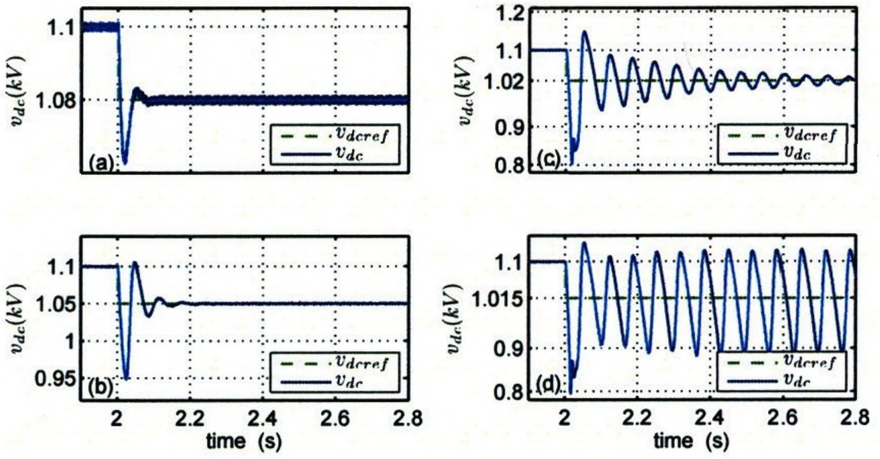

Figure 3.8: Dependence of the PV system dynamics on the operating point if the feed-forward compensation is disabled

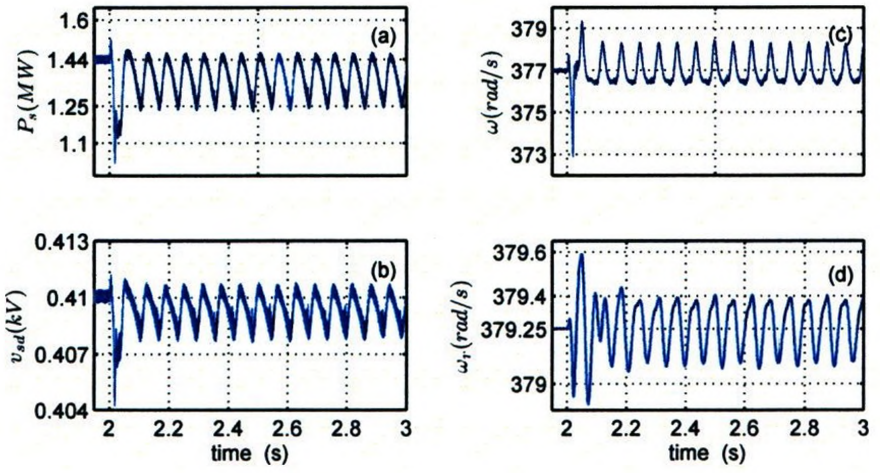

Figure 3.9: Instability of the PV system when the feed-forward compensation is disabled

3.5.6 Power Quality

In view of connection to a distribution network, the impact of a PV system on the power quality is of high importance. To evaluate this impact, the following case study is conducted in which the harmonic spectrum of the current injected into the distribution network is examined. The study is carried out under the condition that $v_{dc} = 1.1\ kV$ and $S = 1$, resulting in an output power of $P_s = 1.34\ MW$.

Fig. 3.10(a) illustrates the spectrum of the VSC AC-side terminal voltage up to the 55^{th} harmonic. It is observed that v_t includes dominant 49^{th}, 51^{st}, and 53^{rd} harmonic components, in addition to its fundamental component. The reason is adoption of a SPWM strategy of which the carrier frequency is 51 times the power line frequency. However, due to the VSC filter, the high-order harmonics are filtered, such that the VSC line current and the current injected into the network have insignificant harmonic distortions, as illustrated in Fig. 3.10(b) and 3.10(c).

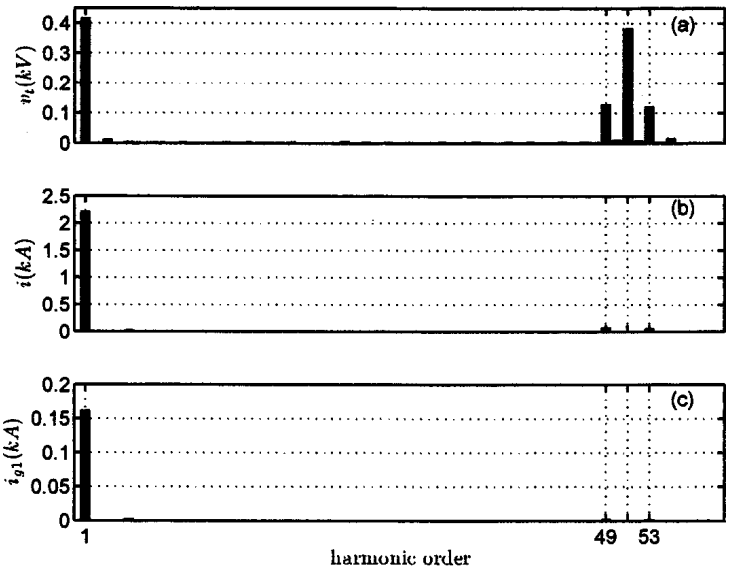

Figure 3.10: Harmonic spectra of v_t, i, and i_{g1}

3.6 Conclusion

In this chapter, the application of the PV system as a distributed generator is demonstrated. The case studies illustrated the need for the feed-forward compensation strategy in maintaining the stability of the PV system under various adverse conditions. Moreover, the case studies revealed the nonlinear characteristic of the PV system when the feed-forward compensation is not in service. It

was further shown that the instability caused in the absence of the feed-forward compensation not only impacts the PV system locally, but also affects the loads connected to the distribution network. Through the case studies it was shown that the decoupled current control is achieved, the PV system is able to maintain the unity power-factor, and the (real) power delivered to the distribution network can be maximized by DC-link voltage control. Moreover in this chapter, the PV system stability under a fault was also examined. Finally, the harmonic spectrum of the current injected into the distribution network was analyzed.

Chapter 4

Modal Analysis of the PhotoVoltaic (PV) System Interfaced with a Distribution Network

4.1 Introduction

Chapter 3 provided a mathematical model of the PhotoVoltaic (PV) system interfaced with a distribution network. Chapter 3 further discussed the performance of the PV system subjected to disturbances in the DC-link voltage level, the insolation level, etc. Moreover, behavior of the system was studied in the presence as well as in the absence of the feed-forward compensation of the DC-link voltage controller. The approach taken in Chapter 3 was a simulation-based one which attempted to provide a better understanding of the PV system and its dynamic properties. However, Chapter 3 did not provide a systematic analytical approach. In this chapter, a small-signal analysis of the PV system of Fig. 2.1 is conducted to characterize the dynamic properties of the PV system, and to characterize the dynamic interactions between the PV system and the distribution network/load.

To evaluate the stability of the PV system under the proposed control strategy, and to investigate the potential for interactions between the PV system and the distribution network/load, an eigenvalue analysis is carried out. The analysis is based on a linearized state-space model of the overall system. The parameters of the linearized model are functions of the steady-state operating point.

4.2 Small-Signal Model

4.2.1 Linearization

The models of the PV system, the distribution network, and the load developed in Chapter 2 and Chapter 3 are nonlinear. Nonlinear equations are suitable for large-signal analysis and simulation studies. Simulation studies provide an insight into the behavior of the PV system in response to disturbances. However, they are not very useful in providing information about the system stability, and robustness against parameters uncertainties. Furthermore, it can not readily be understood from the nonlinear equations as to how each dynamic mode is influenced by different parameters, e.g. the insolation level, length of distribution line, X/R ratio, etc. Therefore, the nonlinear equations are linearized about a system steady-state operating point, to provide a linear model. Of course, the derived linear model is valid only for small perturbations of the system around the operating point.

For the purposes of modeling and analysis, the system of Fig. 3.1 is categorized into three subsystems: the PV subsystem ($\mathbf{X}_c$), distribution network subsystem ($\mathbf{X}_n$), and load subsystem ($\mathbf{X}_l$). Eigenvalue analysis is performed on the linearized model of the overall system which includes the foregoing three subsystems. The three subsystems are governed by the following nonlinear equations.

- PV subsystem

$$\dot{\mathbf{X}}_c = \mathbf{f}(\mathbf{X}_c, \mathbf{u}_c) \tag{4.1}$$

where

$$\mathbf{X}_c = \begin{bmatrix} i_d & v_{dc}^2 & x_3 & x_4 & i_q & x_6 & x_7 & \rho \end{bmatrix}^T \tag{4.2}$$

$$\mathbf{u}_c = \begin{bmatrix} v_{sd} & v_{sq} & v_{dcref}^2 & i_{qref} & S \end{bmatrix}^T \tag{4.3}$$

- Distribution Network subsystem

$$\dot{\mathbf{X}}_n = \mathbf{f}(\mathbf{X}_n, \mathbf{u}_n) \tag{4.4}$$

where

$$\mathbf{X}_n = \begin{bmatrix} i_{g1d} & i_{g1q} & i_{g2d} & i_{g2q} & v_{sd} & v_{sq} & v_{ld} & v_{lq} \end{bmatrix}^T \tag{4.5}$$

$$\mathbf{u}_n = \begin{bmatrix} i_d & i_q & \omega & \rho & i_{ld} & i_{lq} \end{bmatrix}^T \tag{4.6}$$

- Load subsystem

$$\dot{\mathbf{X}}_l = \mathbf{f}(\mathbf{X}_l, \mathbf{u}_l) \tag{4.7}$$

where

$$\mathbf{X}_l = \begin{bmatrix} i_{1d} & i_{1q} & i_{2d} & i_{2q} & \omega_r \end{bmatrix}^T \tag{4.8}$$

$$\mathbf{u}_l = \begin{bmatrix} v_{ld} & v_{lq} & \omega & T_m \end{bmatrix}^T \tag{4.9}$$

The derivation of the nonlinear equations is discussed in Chapters 2 and 3. As an example, let us go through the linearization process for a general nonlinear system described by,

$$\dot{\mathbf{x}} = \mathbf{f}(\mathbf{x}, \mathbf{u}) \tag{4.10}$$

Let $\mathbf{x}_0$, be the initial state vector and $\mathbf{u}_0$, the input vector corresponding to the equilibrium point about which the small-signal performance is to be investigated for the aforementioned nonlinear system described by equation (4.10). Since $\mathbf{x}_0$ and $\mathbf{u}_0$ satisfy equation (4.10), one can deduce

$$\dot{\mathbf{x}}_0 = \mathbf{f}(\mathbf{x}_0, \mathbf{u}_0) = 0 \tag{4.11}$$

If the system is subjected to a small disturbance, there will be perturbation in state variables, so the final perturbed state is

$$\begin{aligned} \mathbf{x} &= \mathbf{x}_0 + \tilde{\mathbf{x}} \\ \mathbf{u} &= \mathbf{u}_0 + \tilde{\mathbf{u}} \end{aligned} \tag{4.12}$$

Substituting the new value of $\mathbf{x}$ and $\mathbf{u}$ from (4.12) in (4.10), one obtains

$$\begin{aligned} \dot{\mathbf{x}} &= \dot{\mathbf{x}}_0 + \dot{\tilde{\mathbf{x}}} \\ &= \mathbf{f}[(\mathbf{x}_0 + \tilde{\mathbf{x}}), (\mathbf{u}_0 + \tilde{\mathbf{u}})] \end{aligned} \tag{4.13}$$

As the perturbations are assumed to be small, the nonlinear function $\mathbf{f}(\mathbf{x}, \mathbf{u})$ can be expressed in terms of Taylor's series expansion. With terms involving second

or higher orders of $\widetilde{x}, \widetilde{u}$ neglected. When Taylor's series is applied on the function, $\mathbf{f}(\mathbf{x}, \mathbf{u})$, it becomes

$$\begin{aligned}\dot{x}_i = \dot{x}_{i0} + \dot{\widetilde{x}}_i &= f_i\left[(\mathbf{x}_0 + \widetilde{\mathbf{x}}), (\mathbf{u}_0 + \widetilde{\mathbf{u}})\right] \\ &= f_i(\mathbf{x}_0, \mathbf{u}_0) + \frac{\partial f_i}{\partial x_1}\widetilde{x}_1 + \ldots + \frac{\partial f_i}{\partial x_n}\widetilde{x}_n + \frac{\partial f_i}{\partial u_1}\widetilde{u}_1 + \ldots + \frac{\partial f_i}{\partial u_r}\widetilde{u}_r\end{aligned} \tag{4.14}$$

Since $\dot{x}_{i0} = f_i(\mathbf{x}_0, \mathbf{u}_0)$, one deduces

$$\dot{\widetilde{x}}_i = \frac{\partial f_i}{\partial x_1}\widetilde{x}_1 + \ldots + \frac{\partial f_i}{\partial x_n}\widetilde{x}_n + \frac{\partial f_i}{\partial u_1}\widetilde{u}_1 + \ldots + \frac{\partial f_i}{\partial u_r}\widetilde{u} \tag{4.15}$$

with i=1,2,.....,n one can have

$$\dot{\widetilde{\mathbf{x}}}_i = \mathbf{A}\widetilde{\mathbf{x}} + \mathbf{B}\widetilde{\mathbf{u}} \tag{4.16}$$

$$\mathbf{A} = \begin{bmatrix} \frac{\partial f_1}{\partial x_1} & \cdots & \frac{\partial f_1}{\partial x_n} \\ \cdots & \cdots & \cdots \\ \frac{\partial f_n}{\partial x_1} & \cdots & \frac{\partial f_n}{\partial x_n} \end{bmatrix} \tag{4.17}$$

$$\mathbf{B} = \begin{bmatrix} \frac{\partial f_1}{\partial u_1} & \cdots & \frac{\partial f_1}{\partial u_r} \\ \cdots & \cdots & \cdots \\ \frac{\partial f_n}{\partial u_1} & \cdots & \frac{\partial f_n}{\partial u_r} \end{bmatrix} \tag{4.18}$$

All of the partial derivatives in the matrices **A**, **B** are evaluated at the equilibrium point x_0. Following the procedures from (4.10) to (4.16) linearization of PV subsystem, distribution network subsystem and load subsystem are carried out.

4.2.2 Linearized Model of the PV Subsystem

As discussed in Chapter 2, the mathematical model of the PV system is represented by a set of nonlinear equations. Appendix C presents a detailed procedure of linearizing these equations based on (4.10) to (4.16). Equations (C.23), (C.28), (C.16), C.17, (C.24), (C.29), (C.30) and (C.31) from Appendix C represent the linearized equations in state variables $\tilde{X}_1$, $\tilde{X}_2$, $\tilde{X}_3$, $\tilde{X}_4$, $\tilde{X}_5$, $\tilde{\xi}_1$, $\tilde{\xi}_2$, $\tilde{\rho}$.

The linearized form for the photovoltaic system can be written in the following form,

$$\frac{d\tilde{\mathbf{X}}_c}{dt} = \mathbf{A}_c\tilde{\mathbf{X}}_c + \mathbf{B}_c\begin{bmatrix} \tilde{v}_{sd} \\ \tilde{v}_{sq} \end{bmatrix} + \mathbf{C}_c\begin{bmatrix} \tilde{v}_{dcref} \\ \tilde{i}_{qref} \\ \tilde{S} \end{bmatrix} \tag{4.19}$$

$$\begin{bmatrix} \tilde{i}_d \\ \tilde{i}_q \end{bmatrix} = \mathbf{D}_c\tilde{X}_c \tag{4.20}$$

$$\tilde{\omega} = \mathbf{E}_c\tilde{X}_c \tag{4.21}$$

$$\tilde{\rho} = \mathbf{F}_c\tilde{X}_c \tag{4.22}$$

Equations (4.19) through (4.22) constitute a linearized state-space model for the PV subsystem. For the PV subsystem, $\tilde{v}_{sd}$ and $\tilde{v}_{sq}$ are the inputs obtained from the distribution network subsystem, whilst $\tilde{i}_d$, $\tilde{i}_q$, $\tilde{\omega}$ and $\tilde{\rho}$ are the outputs delivered to the distribution network subsystem. There is no direct coupling between the PV subsystem and the load subsystem.

4.2.3 Linearized Model of the Distribution Network Subsystem

Dynamics of distribution network in *dq*-frame are described by (3.5) to (3.12) in Chapter 3. The linearized equations of distribution network subsystem are presented in Appendix D. Equations (D.1) through (D.8) can be represented in state-space form as:

$$\frac{d\tilde{\mathbf{X}}_n}{dt} = \mathbf{A}_n\tilde{\mathbf{X}}_n + \mathbf{B}_n\begin{bmatrix}\tilde{i}_d\\ \tilde{i}_q\end{bmatrix} + \mathbf{C}_n\tilde{\omega} + H_n\tilde{\rho} + \mathbf{D}_n\begin{bmatrix}\tilde{i}_{ld}\\ \tilde{i}_{lq}\end{bmatrix} \tag{4.23}$$

$$\begin{bmatrix}\tilde{v}_{ld}\\ \tilde{v}_{lq}\end{bmatrix} = \mathbf{E}_n\tilde{\mathbf{X}}_n \tag{4.24}$$

$$\begin{bmatrix}\tilde{v}_{sd}\\ \tilde{v}_{sq}\end{bmatrix} = \mathbf{F}_n\tilde{\mathbf{X}}_n \tag{4.25}$$

where

$$\tilde{\mathbf{X}}_n = \begin{bmatrix}\tilde{i}_{g1d} & \tilde{i}_{g1q} & \tilde{i}_{g2d} & \tilde{i}_{g2q} & \tilde{v}_{sd} & \tilde{v}_{sq} & \tilde{v}_{ld} & \tilde{v}_{lq}\end{bmatrix}^T \tag{4.26}$$

Equations (4.23) to (4.25) constitute a linear state-space model of the distribution network subsystem. $\tilde{i}_d$, $\tilde{i}_q$, $\tilde{\omega}$, and $\tilde{\rho}$ are the inputs obtained from the PV subsystem, whereas $\tilde{i}_{ld}$ and i_{lq} are the inputs obtained from the load subsystem. $\tilde{v}_{ld}$ and $\tilde{v}_{lq}$ are the outputs delivered to the load subsystem; and $\tilde{v}_{sd}$ and $\tilde{v}_{sq}$ are the outputs delivered to the PV subsystem. It should be noted that $\tilde{\rho}$ represents the perturbation of the phase angle of v_{sabc} relative to that of the grid voltage v_{gabc}. The steady-state value of ρ, is determined based on the real- and reactive-power flow in the system.

4.2.4 Linearized Model of the Load subsystem

In Section 3.4 the mathematical model of a squirrel-cage asynchronous machine was presented. Appendix E contains the linearized expressions of equations describing the dynamics of the asynchronous machined load. The state-space representation of (E.1) through (E.5) is:

$$\frac{d}{dt}\tilde{\mathbf{X}}_l = \mathbf{A}_l\tilde{\mathbf{X}}_l + \mathbf{B}_l\begin{bmatrix}\tilde{v}_{ld}\\ \tilde{v}_{lq}\end{bmatrix} + \mathbf{C}_l\tilde{\omega} + \mathbf{D}_l\tilde{T}_m \tag{4.27}$$

$$\begin{bmatrix}\tilde{i}_{ld}\\ \tilde{i}_{lq}\end{bmatrix} = \mathbf{E}_l\tilde{\mathbf{X}}_l \tag{4.28}$$

where

$$\tilde{\mathbf{X}}_l = \begin{bmatrix}\tilde{i}_{1d} & \tilde{i}_{1q} & \tilde{i}_{2d} & \tilde{i}_{2q} & \tilde{\omega}_r\end{bmatrix}^T \tag{4.29}$$

Equations, (4.27)-(4.29), represent the linearized model of the load. Mechanical torque, $\tilde{T}_m$ is the free control input for the asynchronous machine. However, the control input as well as other matrices; $\tilde{\mathbf{X}}_l$, $\mathbf{A}_l$, $\mathbf{B}_l$, $\mathbf{C}_l$, $\mathbf{D}_l$, $\mathbf{E}_l$ have different entries and dimensions depending on the type of load. Two other types of loads are discussed in the next chapter. In the linearized model of asynchronous load, $\tilde{v}_{ld}$ and $\tilde{v}_{lq}$ are the inputs obtained from the distribution network subsystem, and $\tilde{\omega}$ is the input obtained from the PV subsystem. On the other hand, $\tilde{i}_{ld}$ and $\tilde{i}_{lq}$ are the outputs delivered to the distribution network subsystem.

4.3 Linearized Model of Overall System

The linearized model of overall system is derived by combining three subsystems discussed in subsections 4.2.2 to 4.2.4. The final linearized model is achieved by substituting the output(s) of a subsystem in the relevant input(s) of another subsystem. The process yields

$$\frac{d\tilde{\mathbf{X}}_{sys}}{dt} = \underbrace{\begin{bmatrix} \mathbf{A}_c & \mathbf{B}_c\mathbf{F}_n & 0_{8\times m} \\ (\mathbf{B}_n\mathbf{D}_c + \mathbf{C}_n\mathbf{E}_c + \mathbf{H}_n\mathbf{F}_c) & \mathbf{A}_n & \mathbf{D}_n\mathbf{E}_l \\ \mathbf{C}_l\mathbf{E}_c & \mathbf{B}_l\mathbf{E}_n & \mathbf{X}_l \end{bmatrix}}_{A_{sys}} \tilde{\mathbf{X}}_{sys} + \mathbf{B}_{sys}\tilde{\mathbf{U}}_{sys} \tag{4.30}$$

where,

$$\tilde{\mathbf{U}}_{sys} = \begin{bmatrix} \tilde{v}_{dcref} & \tilde{S} & \tilde{i}_{qref} & \tilde{u}_l \end{bmatrix}^T \tag{4.31}$$

$$\tilde{\mathbf{X}}_{sys} = \begin{bmatrix} \tilde{\mathbf{X}}_c^T & \tilde{\mathbf{X}}_n^T & \tilde{\mathbf{X}}_l^T \end{bmatrix}^T \tag{4.32}$$

An output of interest can be expressed as

$$y = \mathbf{C}_{sys}\tilde{\mathbf{X}}_{sys} \tag{4.33}$$

Equation (4.30) has 21 state variables, if the load is an asynchronous machine. Each eigenvalue corresponds to one of the system modes. The PV subsystem of Fig. 2.1 has 8 modes, the distribution network subsystem also has 8 modes, and load subsystem has m modes. Thus, depending on the type of load, the number of eigenmodes of the load subsystem varies. Based on the first theorem of Lyapunov, the stability of the system is determined by the eigenvalues of the system as follows [39]:

- If the real parts of all eigenvalues are negative, the system is asymptotically stable around the equilibrium point;
- If at least one of the eigenvalues has a positive real part, the system is unstable; and
- If at least one eigenvalue has a zero real part, the system stability around the equilibrium point can not be judged.

To determine the contribution of each variable in a mode and to evaluate the sensitivity of the mode to system parameters, a participation factor analysis [39]-[40] is also conducted in this chapter.

4.4 Model Verification

The linearized model of (4.30) is implemented in MATLAB software environment with the parameters specified in Tables A.1-A.3. The results obtained from MATLAB are compared with those of the detailed switched model of the system implemented in PSCAD/EMTDC environment to evaluate the accuracy of the linearized model. The accuracy of the linearized model is evaluated for both conditions of disabled and enabled feed-forward compensation in the DC-link voltage control loop.

4.4.1 Case 1: Step change in DC-link voltage

Initially, the system of Fig. 4.1 is in a steady state, and the reference commands v_{dcref} and i_{qref} are set to 1.0 kV and zero, respectively. In addition, the feed-forward compensation of the DC-link voltage controller is enabled. The load is

connected to the middle of the distribution line, i.e. d_f = 0.5. The machine is used as a generator with a mechanical torque of −0.71 pu. At t=2.0 s, a 10% step change is imposed on v_{dc}. Fig. 4.1 illustrates the response of the DC-link voltage to the disturbance at insolation levels of S =0.1, 0.5, and 1.0. The columns (a) and (b) of Fig. 4.1 illustrate the responses obtained from the linearized model and the switched model, respectively. It can be observed that the linearized model closely agrees with the detailed switched model.

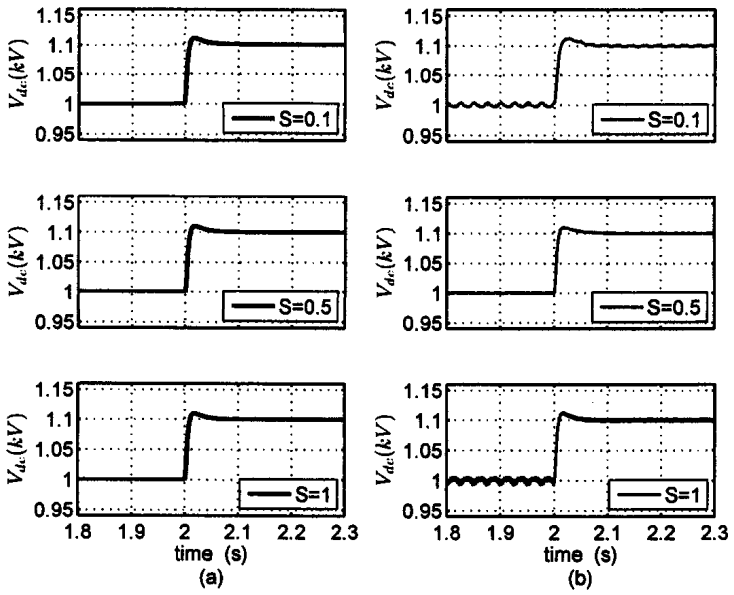

Figure 4.1: Step response of the DC-link voltage obtained from (a) linearized model, and (b) switched model

Fig. 4.2 illustrates the responses of i_d and P_s to the aforementioned disturbance, only for the unity insolation level. Similar to Fig. 4.1, column (a) includes the response based on the linearized model, whereas column (b) illustrates that obtained from the switched model. Fig. 4.2 shows that subsequent to the disturbance, i_d increases from 2.22 to 2.31 kA, corresponding to a change in the real power P_s from 1.35 to 1.41 MW. Fig. 4.2 also confirms the close agreement between the linearized model and the switched model.

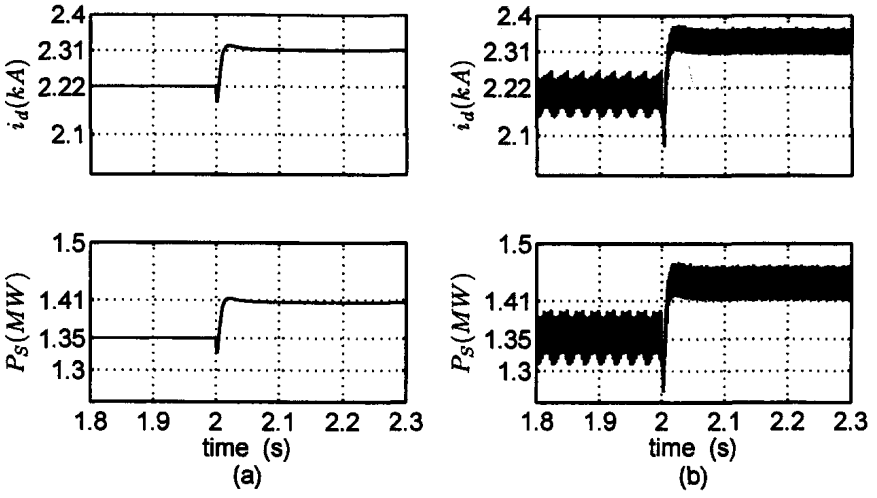

Figure 4.2: Response of i_d and P_s to a step change in DC-link voltage (a) linearized model, and (b) switched mo

4.4.2 Case 2: Effectiveness of Feed-Forward Compensation

This case was already discussed in Section 3.5. Here, the oscillations caused by deactivation of the feed-forward compensation at $v_{dcref} = 1.015\ kV$, are examined from a modal analysis perspective.

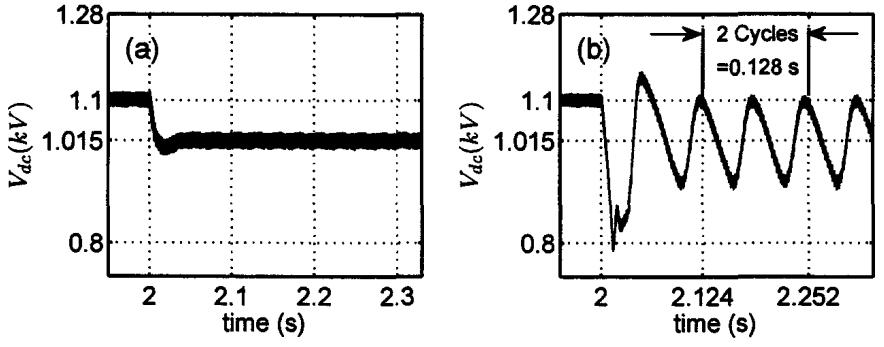

Figure 4.3: Step response of DC-link voltage;(a) with feed-forward compensation, and (b) without feed-forward compensation

Fig. 4.3(a) illustrates the response of v_{dc} to the disturbance when the feed-forward compensation is in service. Fig. 4.3(b) illustrates the response of v_{dc} when the feed-forward compensation is disabled. Fig. 4.3(b) shows that sub-

sequent to the disturbance, the response becomes oscillatory with a frequency of about 15.6 Hz. On the other hand calculation of the system eigenvalues for this case, based on equation (4.30), reveals the existence of a pair of complex-conjugate eigenvalues at $8.5 \pm 100.1j$ for this case. The imaginary part of the eigenvalues corresponds to a 15.9 Hz oscillatory mode, which is in a close agreement with the response obtained from switched model, Fig. 4.3(b).

4.5 Eigenvalue and Sensitivity Analyses

To identify the potential interactions between the PV system and the distribution network/loads, to identify the nature of interactions, and to determine the robustness of the PV system controllers against variation of parameters, an eigenvalue analysis is carried out on the linearized model of (4.30). The system parameters are reported in Tables A.1-A.6. The analysis indicates that, under the proposed control strategy, the PV system dynamics possess more or less the same properties irrespective of the parameters variation. Table 4.1 illustrates the results which are discussed hereafter.

Table 4.1 reports the eigenvalues of the overall system, i.e. the solution of $|\mathbf{A}_{sys} - \lambda_i I| = 0$ (i=1, 2, ...,8+8+m), under the condition that the feed-forward compensation is enabled. The eigenvalues are calculated for $\gamma = 1$, $l_e = 15$ km, $X/R = 0.6$, and $d_f = 0.5$. In addition, the DC-link voltage is 1.1 kV. Table 4.1 shows the eight eigenvalues of the PV subsystem, of which the first five correspond to the VSC whereas the other three are due to the PLL. Out of the eight eigenvalues of the distribution network subsystem, only the dominant one is reported here. Similarly, the eigenvalue corresponding to the load is also the

Table 4.1: Overall System Eigenvalues and States Participation Factors; $\gamma = 1$, $l_e = 15\ km$, $X/R = 0.6$, $d_f = 0.5$.

		Eigenvalues of $\mathbf{A}_{sys}$ and Their Associated Subsystems								
		λ_1 = -1350; PV	λ_2 = -672; PV	λ_3 = -228; PV	λ_4 = -55; PV	λ_5 = -2000; PV	λ_6 = - 132.5; PV	$\lambda_{7,8}$ = $-219 \pm 111j$; PV	$\lambda_{9,10}$ = $-143 \pm 8437j$; Network	λ_{11} = $-29 \pm 0.4j$; Load
PV System States	$\tilde{X}_{c1}$	0.760	0.163	0.110	0.007	0	0.007	0.007	0.007	≈ 0
	$\tilde{X}_{c2}$	0.020	0.620	2.090	0.044	0	0.022	0.033	≈ 0	≈ 0
	$\tilde{X}_{c3}$	0.001	0.042	0.479	1.420	0	0.011	0.006	≈ 0	≈ 0
	$\tilde{X}_{c4}$	0.087	1.770	0.698	0.027	0	0.004	0.011	≈ 0	≈ 0
	$\tilde{X}_{c5}$	0	0	0	0	1	0	0	0	0
	$\tilde{X}_{c6}$	0.002	0.003	0.230	≈ 0	0	0.920	1.910	0.002	≈ 0
	$\tilde{X}_{c7}$	≈ 0	≈ 0	0.153	≈ 0	0	3.220	1.073	≈ 0	≈ 0
	$\tilde{X}_{c8}$	0.001	≈ 0	0.353	≈ 0	0	3.090	2.890	0.001	0.012
Network States	$\tilde{X}_{n1}$	0.329	0.033	0.010	≈ 0	0	0.001	0.002	0.006	≈ 0
	$\tilde{X}_{n2}$	≈ 0	≈ 0	≈ 0	≈ 0	0	≈ 0	≈ 0	0.393	≈ 0
	$\tilde{X}_{n3}$	0.034	0.003	0.001	≈ 0	0	≈ 0	≈ 0	0.003	≈ 0
	$\tilde{X}_{n4}$	≈ 0	≈ 0	≈ 0	≈ 0	0	0.002	0.004	0.0913	≈ 0
	$\tilde{X}_{n5}$	0.007	≈ 0	≈ 0	≈ 0	0	≈ 0	≈ 0	0.014	≈ 0
	$\tilde{X}_{n6}$	0.001	≈ 0	≈ 0	≈ 0	0	0.001	0.001	0.456	≈ 0
	$\tilde{X}_{n7}$	≈ 0	≈ 0	≈ 0	≈ 0	0	≈ 0	≈ 0	0.001	≈ 0
	$\tilde{X}_{n8}$	≈ 0	≈ 0	≈ 0	≈ 0	0	0.001	0.002	0.032	≈ 0
Load States	$\tilde{X}_{l1}$	≈ 0	≈ 0	0.006	≈ 0	0	0.033	0.045	≈ 0	0.004
	$\tilde{X}_{l2}$	≈ 0	≈ 0	≈ 0	≈ 0	0	0.001	0.001	0.001	0.005
	$\tilde{X}_{l3}$	≈ 0	≈ 0	0.003	≈ 0	0	0.064	0.0521	≈ 0	0.500
	$\tilde{X}_{l4}$	≈ 0	≈ 0	0.001	≈ 0	0	0.005	0.003	≈ 0	0.504

dominant one. Table 4.1 also shows the state-variables of the overall system as well as a measure of the participation of each state-variable in the eigenmodes corresponding to the eigenvalues.

The participation of a state-variable $\tilde{x}_r$ in a mode corresponding to the eigenmode λ_i is calculated from:

$$p_{ri} = \mathbf{v}_i^r \mathbf{u}_i^r \tag{4.34}$$

where $\mathbf{u}_i^r$ and $\mathbf{v}_i^r$ signify the r^{th} elements of the vectors $\mathbf{u}_i$ and $\mathbf{v}_i$, respectively [38]. $\mathbf{u}_i$ and $\mathbf{v}_i$ are, in turn, the eigenvectors of $\mathbf{A}_{sys}$ and $\mathbf{A}_{sys}^T$, respectively, corresponding to the eigenvalue λ_i. In general, $p_{ri} = a + jb$ is a complex number. However, here the relative participation of a state-variable in a mode is of prime interest and, therefore, $\|p_{ri}\| = \sqrt{a^2 + b^2}$ is reported in Table 4.1 rather than p_{ri}. In addition, the values are rounded off to the thousandth place and any relative participation smaller than 0.001 is denoted by "≈ 0" in the table.

Table 4.1 indicates that while the state-variables of the PV system actively participate in the eigenmodes corresponding to λ_1 to λ_8, participation of the network and load state variables in those eigenmodes is insignificant. The only exception is the network state-variable, $\tilde{X}_{n1}$, which participates relatively actively in the eigenmode corresponding to λ_1. Thus, it can be concluded that the PV subsystem eigenvalues and the corresponding eigenmodes are weak functions of the network and load parameters. Therefore, if the eigenmodes of the PV subsystem are stable by proper design of the controllers, they do not become unstable as a result of variations in the network and load parameters. The participation of $\tilde{X}_{n1}$ in the eigenmode corresponding to λ_1 cannot pose any instability complications, since this mode is very far from the imaginary axis of s-plane. It should be noted that p_{ri} also represents the sensitivity of the eigenvalue λ_i to the element a_{rr} of the system matrix $\mathbf{A}_{sys}$ [41]. Table 4.1 further confirms that the eigenvalues of the PV subsystem, i.e. λ_1 to λ_8, are insensitive to those elements of $\mathbf{A}_{sys}$ that correspond to the network and load subsystems, i.e. a_{rr} with $r = 9, 10, ..., 16 + m$.

Similar analyses are carried out also for an R-L load and a rectifier load, which are discussed in the next chapter.

Participation-factor analysis is conducted also for the case where the system becomes oscillatory in the absence of the feed-forward compensation. This case was discussed in more detail in Section 2.5.2. Table 4.2 indicates the participation of the state variables corresponding to the eigenvalue in the eigenmode $\lambda_8 = 8.5 \pm 100.1j$. Table 4.2 shows that the participation of state variables $\tilde{X}_{c2}$, $\tilde{X}_{c3}$ and $\tilde{X}_{c3}$ is quite significant as compared to the others. In other words, they exhibit the largest contribution to the oscillatory mode of the system at the corresponding operating point. The linearized model suggest that the foregoing state variables are tightly related to the DC-link voltage controller.

Table 4.2: Participation of State-Variables in the Oscillatory Eigenmode, $\lambda_8 = 8.5 \pm 100.1j$

States	Participation	States	Participation	States	Participation	States	Participation
$\tilde{X}_{c1}$	0.007	$\tilde{X}_{c6}$	0.01	$\tilde{X}_{n3}$	0.006	$\tilde{X}_{n8}$	≈ 0
$\tilde{X}_{c2}$	0.6	$\tilde{X}_{c7}$	0.002	$\tilde{X}_{n4}$	≈ 0	$\tilde{X}_{l1}$	0.0015
$\tilde{X}_{c3}$	0.5	$\tilde{X}_{c8}$	0.004	$\tilde{X}_{n5}$	≈ 0	$\tilde{X}_{l2}$	≈ 0
$\tilde{X}_{c4}$	0.15	$\tilde{X}_{n1}$	0.029	$\tilde{X}_{n6}$	≈ 0	$\tilde{X}_{l3}$	0.005
$\tilde{X}_{c5}$	0	$\tilde{X}_{n2}$	≈ 0	$\tilde{X}_{n7}$	≈ 0	$\tilde{X}_{l4}$	≈ 0

The movement of the eigenvalue λ_8 can be explained with reference to the matrix, A_c,(4.19). The diagonal element a_{22} of A_c is equal to -875 when the feed-forward compensation is in service at $v_{dc0} = 1.1$ kV. However, elimination of the feed-forward compensation makes a_{22} equal to 223 at v_{dc0}=1.015 kV. The absence of feed-forward compensation combined with a change of the voltage level has a major impact on the value of a_{22}. Equation (C.28), Appendix

C, formulates the value of a_{22}, in the presence and absence of the feed-forward compensation, respectively, as:

$$(a_{22})_{\gamma=1} = \frac{i_{pv0}}{Cv_{dc0}} - \frac{\mu}{C} - \frac{Li_{d0}}{Cv_{sd}\tau_i} - \frac{i_{pv0}Li_{d0}}{Cv_{sd0}v_{dc0}\tau_i} \tag{4.35}$$

$$(a_{22})_{\gamma=0} = \frac{i_{pv0}}{Cv_{dc0}} - \frac{\mu}{C} \tag{4.36}$$

where the parameter μ is defined in Appendix C. The quantity, $\frac{Li_{d0}}{Cv_{sd}\tau_i} - \frac{i_{pv0}Li_{d0}}{Cv_{sd0}v_{dc0}\tau_i}$, is considerably larger than $\frac{i_{pv0}}{Cv_{dc0}} - \frac{\mu}{C}$. Hence, when $\gamma = 1$ a_{22} takes a negative value and results in an eigenmode in the left half plane, far from the origin. However, this is not the case when the feed-forward compensation is disabled, i.e. $\gamma = 0$. a_{22} becomes equal to $\frac{i_{pv0}}{Cv_{dc0}} - \frac{\mu}{C}$ which is a function of v_{dc0}.

Dominant eigenmodes, $\lambda_3 = -228$ and $\lambda_4 = -55$, are resulted in the PV subsystem for the case when the feed-forward compensation is active. State variables corresponding to the DC-link voltage controller have the highest contribution in the aforementioned dominant eigenmodes as presented in Table 4.1. Table 4.1 conveys the information that, in the dominant mode λ_3, the participation of PLL state variables are quite significant as compared to the eigenmode λ_4. The reason is that presence of feed-forward compensation tends to decouple the voltage control loop from the rest of the system. However, the decoupling is no longer maintained in the absence of feed-forward compensation and a complex conjugate eigenmode, $\lambda_8 = 8.5 \pm 100.1j$ is resulted with significant participation of state variables that correspond to the DC-link voltage control loop and the PLL . Variations of λ_3, λ_4, and λ_8 with respect to v_{dc0} are plotted in Fig. 4.4.

Fig. 4.4(a) plots the variation of the real part of the PV system dominant eigenmode as a function of v_{dc0} when feed-forward compensation is disabled.

Fig. 4.4(c) shows that with the increase in v_{dc0}, the dominant eigenmode moves to the left of the s-plane. A positive real part is resulted if v_{dc0} is reduced to about 1.015 kV. The dominant eigenmodes are also plotted for the case when the feed-forward compensation of the DC-link voltage regulator is active. Figs. 4.4(b) and (c) illustrate that v_{dc0} has insignificant impact on dominant eigenmodes. Hence, the proposed control strategy with feed-forward compensation in the DC-link voltage regulator serves the best purpose for maintaining the stability under various operating conditions.

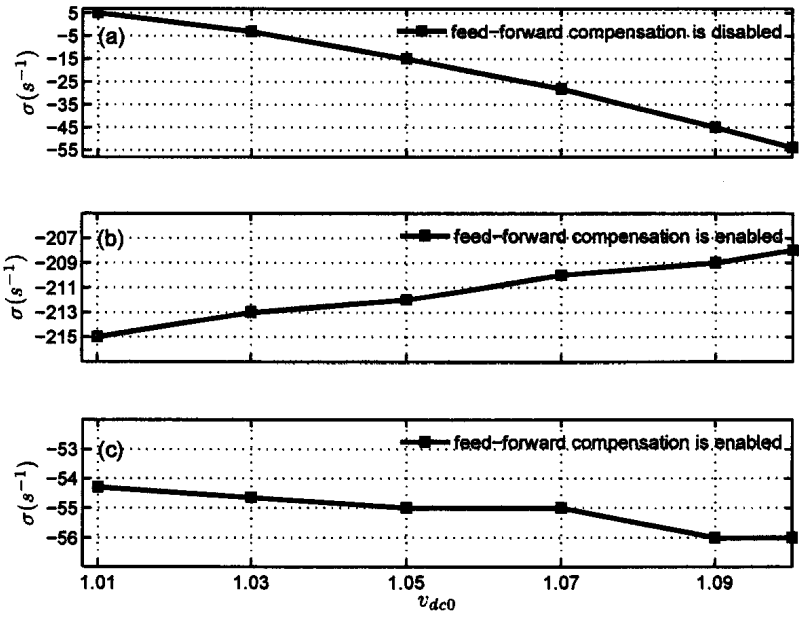

Figure 4.4: Patterns of variation for the PV system eigenvalues as a function of DC-link voltage both in the presence and absence of feed-forward compensation

Figs. 4.5 to 4.8 illustrate the patterns of variation of the real-part of the system eigenvalues, as a function of various parameters. Thus, only the eigenvalues with noticeable variations are considered; the other eigenvalues are found to be almost fixed at their original locations. Fig. 4.5 illustrates the eigenvalue variations as a function of the load distance from the PV system, i.e. d_f. Thus, a value very

close to zero (unity) d_f corresponds to the case where the load is at the PV system (substation) terminals.

Fig. 4.5 shows that (only) one of the eigenvalues of the network subsystem gets closer to the imaginary axis of the s-plane, as the distance between the load and the PV system increases. Nonetheless, the corresponding mode remains stable and fast.

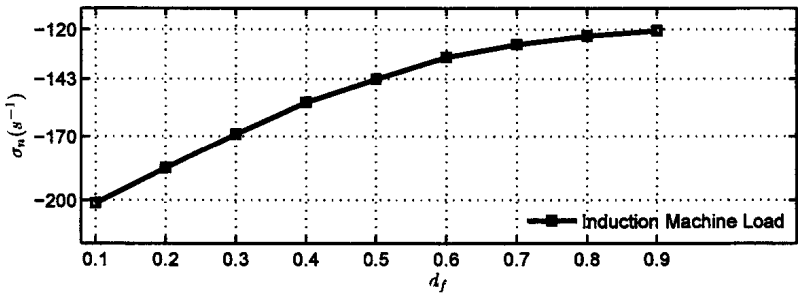

Figure 4.5: Eigenvalue location for a network mode as a function of the load distance from the substation

Fig. 4.6 illustrates the movements of a network eigenvalue and a PV system eigenvalue as functions of the line length l_e, ranging from 5 to 40 km. As Fig. 4.6 indicates, as the line length increases the network eigenmode becomes more stable whereas the PV system eigenvalue moves slightly to the right. This mode of the PV system is very far from the imaginary axis of the s-plane, and its movement to the right cannot cause any instability issues. The change of the PV system eigenvalue is less than 10% as Fig. 4.6 shows.

Fig. 4.7 shows the loci of a network eigenvalue and a PV system eigenvalue, as a function of the line X/R ratio. Fig. 4.7 illustrates that one of the modes become more stable as the X/R ratio increases, whereas the other one exhibits an opposite pattern. As understood from Table 4.1, when the feed-forward compensation is activated none of the corresponding eigenmodes is a dominant one.

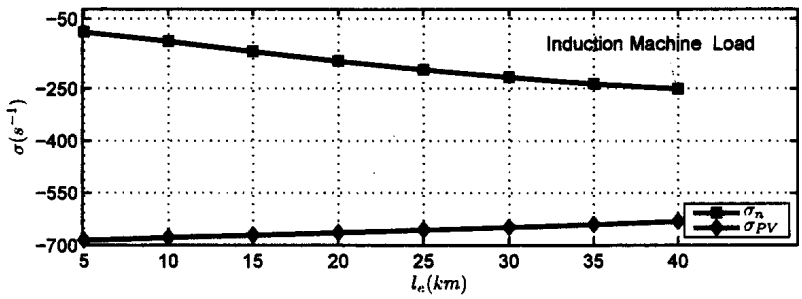

Figure 4.6: Eigenvalues variation as a function of the line length

Nevertheless, both of modes remain stable and very fast. irrespective of the line X/R.

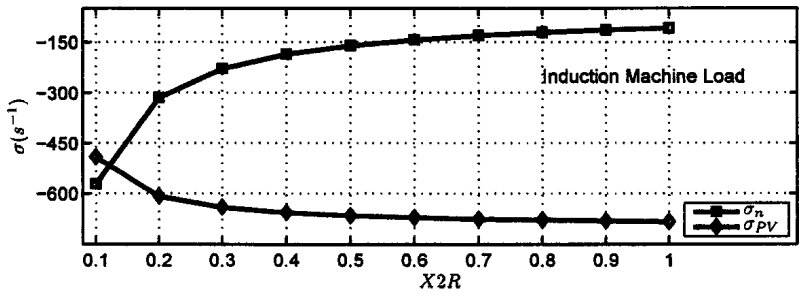

Figure 4.7: Eigenvalues loci as a function of line X/R ratio

The impact of the solar insolation level, S, on the eigenvalues of the PV system is illustrated in Fig. 4.8. Here, (only) two of the PV system modes move as the insolation level changes. In this case, the two modes exhibit opposite patterns of variation as S increases. The modes remain stable and very fast, regardless of the insolation level. There exists no noticeable movement in the eigenvalues of the network and load subsystems due to the insolation level variations, and therefore they are not plotted here.

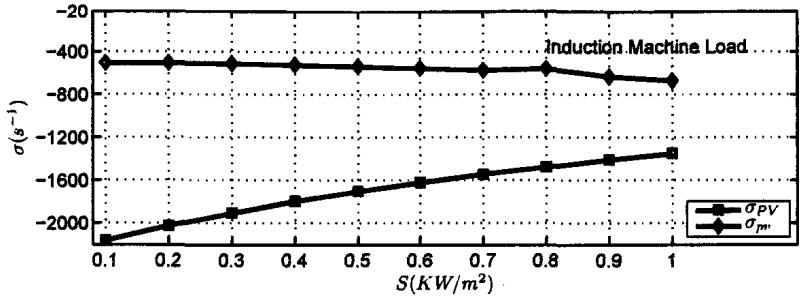

Figure 4.8: Pattern of variation for PV system eigenvalues as a function of insolation level

4.6 Conclusion

This chapter presented a modal/sensitivity analysis on a linearized model that includes the PV subsystem, the distribution network subsystem, and the load subsystem. The modal analysis facilitates characterization of dynamic properties of the PV subsystem, to evaluate the robustness of the controllers, and to identify the interactions between the PV system and the network/loads. The results confirm that, under the proposed control strategy, the dynamics of the PV system are decoupled from those of the distribution network. This, in turn, alternatively means that the PV subsystem does not destabilize the distribution network subsystem.

Chapter 5

Impact of Other Types of Loads on System Dynamics

5.1 Introduction

Chapter 4 introduced a modal analysis for the PV system interfaced with a distribution network which supplied a squirrel-cage induction machine as the load. The results of the modal analysis confirmed that, under the proposed control strategy, dynamics of the PV system are decoupled from those of the distribution network/load. It was further demonstrated that the PV system dynamics are not influenced by the network or the load. This chapter re-evaluates the stability of the PV system as when different types of loads are in the proximity of the PV system. The loads of consideration are: (i) a series $R-L$ load, and (ii) a controlled rectifier load.

5.2 Linearized Model of the Series R-L Load

Fig. 5.1 illustrates the schematic diagram of a three-phase, series, $R-L$ load. To derive a state-space model for the load, the inductor current, which is also the load current, is taken as the state variable. Thus, one can write the equations describing dynamics of the R-L load in the dq-frame as:

$$\frac{di_{ld}}{dt} = -\frac{R_l}{L_l} i_{ld} + \omega i_{lq} + \frac{1}{L_l} v_{ld} \tag{5.1}$$

$$\frac{di_{lq}}{dt} = -\frac{R_l}{L_l} i_{lq} - \omega i_{ld} + \frac{1}{L_l} v_{lq}. \tag{5.2}$$

The linearized form of (5.1) and (5.2) is written as:

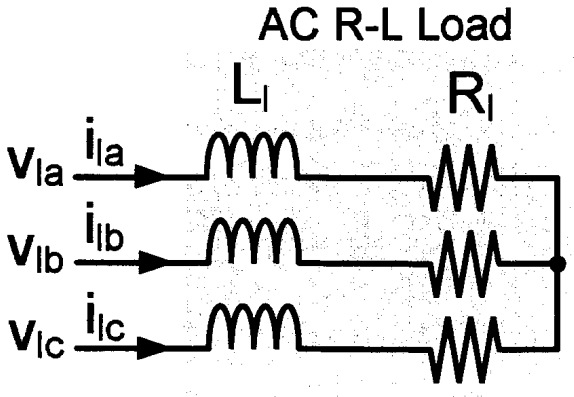

Figure 5.1: Schematic diagram of R-L load

$$\frac{d\tilde{i}_{ld}}{dt} = -\frac{R_l}{L_l}\tilde{i}_{ld} + \omega_0 \tilde{i}_{lq} + \frac{1}{L_l}\tilde{v}_{ld} + i_{lq0}\tilde{\omega} \tag{5.3}$$

$$\frac{di_{lq}}{dt} = -\omega_0 \tilde{i}_{ld} - \frac{R_l}{L_l}\tilde{i}_{lq} + \frac{1}{L_l}\tilde{v}_{lq} - i_{ld0}\tilde{\omega} \tag{5.4}$$

Equations (5.3) and (5.4) can re-written in the compact state-space form:

$$\frac{d}{dt}\tilde{X}_l = A_l \tilde{X}_l + B_l \begin{bmatrix} \tilde{v}_{ld} \\ \tilde{v}_{lq} \end{bmatrix} + C_l \tilde{\omega} + D_l \tilde{U}_l \tag{5.5}$$

$$\begin{bmatrix} \tilde{i}_{ld} \\ \tilde{i}_{lq} \end{bmatrix} = E_l \tilde{X}_l \tag{5.6}$$

where

$$\tilde{X}_l = \begin{bmatrix} \tilde{i}_{ld} & \tilde{i}_{lq} \end{bmatrix}^T. \tag{5.7}$$

Equations (5.5) and (5.6) constitute a linearized model of the series $R-L$ load. In (5.5), there is no free control input as in (2.10), where induction machine, the load. This, in turn, means that D_l is a null matrix. In (5.5), $\tilde{v}_{ld}$ and $\tilde{v}_{lq}$ are the inputs obtained from the distribution network subsystem, and $\tilde{\omega}$ is the input obtained from the PV subsystem. $\tilde{i}_{ld}$ and $\tilde{i}_{lq}$, which are also state-variables of the series R-L load subsystem, are the outputs delivered to the distribution network subsystem. The linearized series $R-L$ load subsystem is incorporated in (4.30) to complement the linearized model of the overall system.

5.3 Linearized Model of the Bridge Rectifier Load

Fig. 5.2 illustrates the schematic diagram of a thyristor-controlled rectifier supplying a series, $R-L$, DC load. If the inductor current is picked as the state variable, then

$$L_{rec}\frac{di_{rec}}{dt} = -R_{rec}i_{rec} + v_{rec} \tag{5.8}$$

where v_{rec} is the rectifier DC-side voltage. It is now assumed that the rectifier operates in the continuous mode, i.e. $i_{rec} \lneq 0$, and L_{rec} is so large that i_{rec} is essentially ripple-free. Thus, v_{rec} can be approximated by its averaged component,

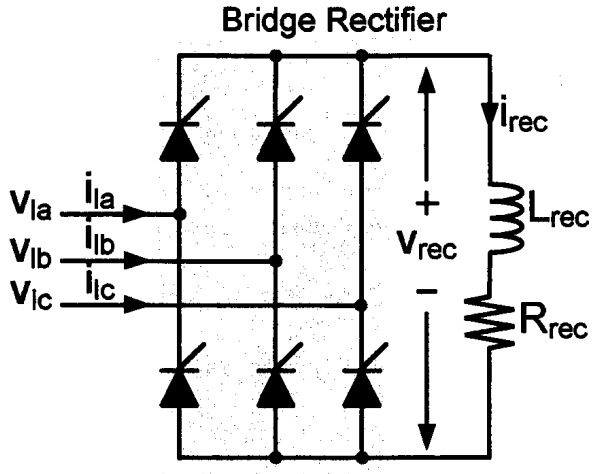

Figure 5.2: Schematic diagram of rectifier load

as

$$v_{rec} \approx \overline{v_{rec}} = \frac{3\sqrt{3}}{\pi}\widehat{v_l}cos\alpha$$
$$= \frac{3\sqrt{3}}{\pi}\sqrt{(Re\{\vec{v_l}\})^2 + (Im\{\vec{v_l}\})^2}cos\alpha \tag{5.9}$$

where α is the firing angle, and $\widehat{v_l}$ is the magnitude of $\vec{v_l}$. Substituting for v_{rec} from (5.9) in (5.8), one finds

$$L_{rec}\frac{di_{rec}}{dt} = -R_{rec}i_{rec} + \frac{3\sqrt{3}}{\pi}\sqrt{(Re\{\vec{v_l}\})^2 + (Im\{\vec{v_l}\})^2}cos\alpha\,. \tag{5.10}$$

An expression for the load current can be derived using the principle of power balance. Thus

$$\frac{3}{2}Re\{\vec{v_l}\,\vec{i_l}^*\} = i_{rec}\overline{v_{rec}}$$
$$= i_{rec}\frac{3\sqrt{3}}{\pi}\underbrace{\sqrt{(Re\{\vec{v_l}\})^2 + (Im\{\vec{v_l}\})^2}}_{\widehat{v_l}}cos\alpha \tag{5.11}$$

The fundamental component of the phase current of a bridge rectifier is delayed by the angle α with respect to the corresponding phase voltage [42]. Therefore,

if $\vec{i_l}$ is approximated by its fundamental component, one can write

$$\vec{i_l} = \hat{i_l}\frac{\vec{v_l}}{\hat{v_l}}e^{-j\alpha} \tag{5.12}$$

where $\hat{i_l}$ is the magnitude of the space-phasor equivalent of the load (fundamental) current; $\vec{v_l}/\hat{v_l}$ is the unit vector collinear with $\vec{v_l}$. Substitution of $\vec{i_l}$ from (5.12) in (5.11), and simplification of the resultant in view of $\vec{v_l}\vec{v_l}^* = \hat{v_l}^2$, yields

$$\hat{i_l} = \frac{2\sqrt{3}}{\pi} i_{rec} \tag{5.13}$$

Substituting for $\hat{i_l}$ from (5.13) in (5.12), one deduces

$$\begin{aligned}\vec{i_l} &= \left(\frac{2\sqrt{3}}{\pi}\right)\frac{\vec{v_l}}{\hat{v_l}}e^{-j\alpha} i_{rec} \\ &= \left(\frac{2\sqrt{3}}{\pi}\right)\frac{\vec{v_l}}{\sqrt{(Re\{\vec{v_l}\})^2 + (Im\{\vec{v_l}\})^2}}e^{-j\alpha} i_{rec}\,.\end{aligned} \tag{5.14}$$

Equations (5.10) and (5.14) constitute a state-space model of the controlled rectifier load in the space-phasor form. Their linearized counterpart can be represented in the dq-frame as:

$$\frac{di_{rec}}{dt} = -\frac{R_{rec}}{L_{rec}} i_{rec} + \frac{3\sqrt{3}}{\pi}\hat{v}_l \cos\alpha \tag{5.15}$$

$$i_{ld} = \frac{2\sqrt{3}}{\pi} i_{rec} \cos\alpha \tag{5.16}$$

$$i_{lq} = \frac{2\sqrt{3}}{\pi} i_{rec} \sin\alpha \tag{5.17}$$

Equations (5.15)-(5.17) can be re-written in the form (5.5)-(5.6), for the completion of the overall system model. It should be noted though that the matrices A_l, B_l, C_l, D_l, and E_l are different than their counterparts for the series, $R - L$, load of Section 5.2.

5.4 Eigenvalue Analyses

Figs. 5.3 to 5.6 demonstrate the variation of the real-part of the system eigenvalues, as a function of various parameters of the series $R-L$ load and the rectifier load. The figures include only those eigenvalues that vary noticeably as compared to the others. Parameters for the series $R-L$ load and rectifier load are provided in Tables A.2 and A.3, respectively. Figs. 5.3(a) and 5.3(b), respectively, illustrate the variation of dominant eigenmode as a function of the load distance from the PV system, i.e. d_f, for series $R-L$ load and rectifier load.

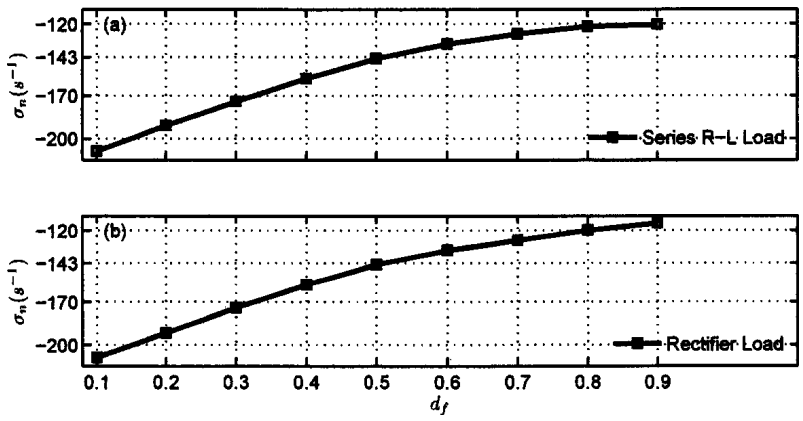

Figure 5.3: Patterns of variation for the PV system eigenvalues as a function of insolation level

Figs. 5.4(a) and 5.4(b), respectively, plot the variation patterns of the dominant eigenmodes as a function of the line length l_e, ranging from 5 to 40 km, for the series $R-L$ load and the rectifier load. The figures indicate that the eigenvalues of the distribution network subsystem and the PV subsystem are the ones that are mostly influenced by line length. the eigenvalues' real-parts indicate that the network eigenmodes becomes more stable as the length increases whereas the PV subsystem eigenmodes move slightly to the right similar to the case where induction machine was used as the load. With the variation of the line X/R ratio,

the loci of the distribution network and load subsystem eigenmodes are illustrated in Figs. 5.5(a) and 5.5(b), for the $R-L$ load and the rectifier load, respectively. The impact of the insolation level, S, on the eigenvalues of the PV system is illustrated in Fig. 5.6. The figure shows that the modes of the distribution network and those of the load remain stable irrespective of variations of the insolation level.

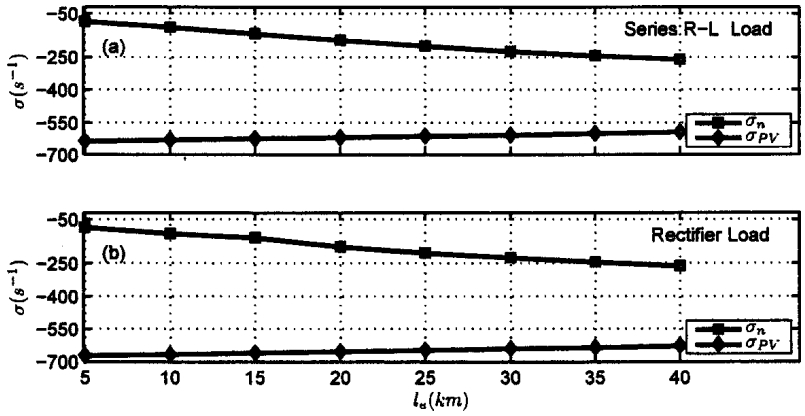

Figure 5.4: Eigenvalues variation as a function of the line length

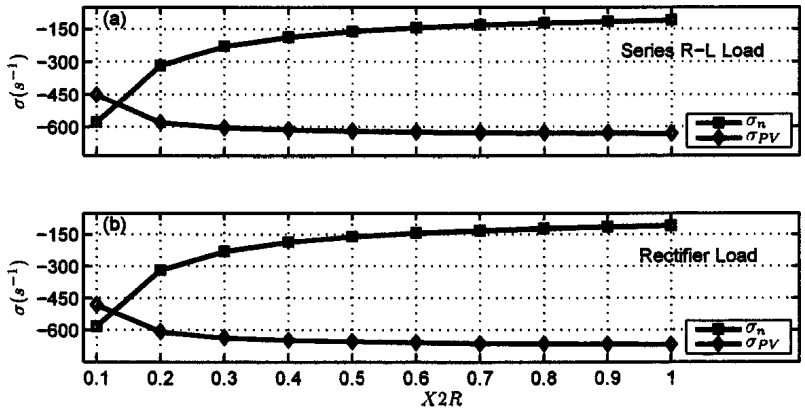

Figure 5.5: Eigenvalues loci as a function of line X/R ratio

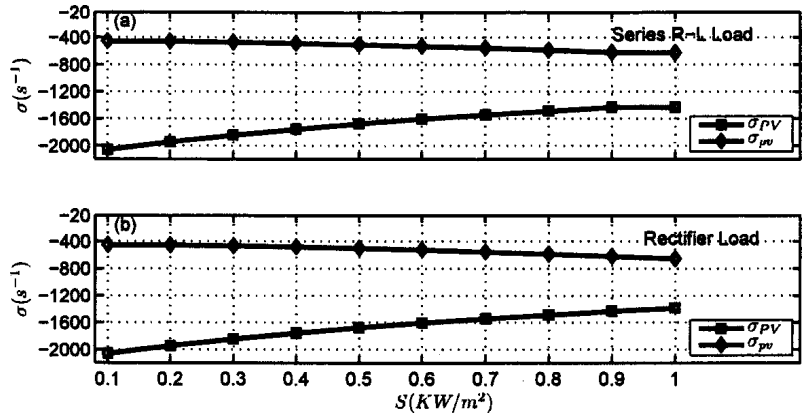

Figure 5.6: Pattern of variation for PV system eigenvalues as a function of insolation level

5.5 Conclusion

This chapter re-evaluated the stability of a PV system that is connected to a distribution network, when two different types of loads are supplied by the network. The results obtained from these two loads are in close agreement with those obtained for the induction machine load. Thus, it can be concluded that the PV system with feed-forward compensation in the DC-link voltage controller maintains its stability and dynamic properties in spite of major variation in the line length, line X/R ratio, solar insolation level, load distance, and, more importantly, the load type.

Although it can be argued that only three types of loads are modeled in this thesis. It should be noted that practical loads in utility systems are often considered as a weighted composition of these three types. Therefore, the results can be relied upon for a real world scenario.

Chapter 6

Summary, Conclusions, and Future Work

6.1 Summary and Conclusions

In this thesis:

- a detailed mathematical model for a single-stage, three-phase PhotoVoltaic (PV) system is decoupled;
- a novel control strategy is proposed which adopts an inner current-control loop and an outer DC-link voltage control loop. The current control mechanism renders the PV system protected against faults and overloads. The DC-link voltage control enables the output power control/maximization;
- a feed-forward compensation mechanism is proposed for the DC-link voltage control loop to mitigate the impact of nonlinear characteristic of the PV matrix, to permit the design and optimization of the DC-link voltage controller for a wide range of operating condition. The effectiveness of the feed-forward compensation is verified through digital time-domain simulations carried out on a detailed switched model of the overall system;

- performance of the developed PV system as a Distributed Generation (DG) is evaluated and most important transients of the PV system are identified;
- a comprehensive modal/sensitivity analysis is conducted for the first time on a linearized model of the overall system i.e. the (PV system, the distribution network , and the load), to evaluate the robustness of the controllers, and to identify potential interactions between the PV system and the network/loads.

The conclusions of the thesis are as follows:

- the feed-forward compensation strategy of the DC-link voltage control loop is very effective in maintaining the stability of the PV system. In the absence of the feed-forward compensation, it is difficult to design a controller that guarantees stability in different power levels;
- the current-control strategy is an effective means of protecting PV system against short-circuit faults and overloads. More importantly, it virtually de-couples the dynamics of the PV system and those of distribution network;
- under proposed control strategy, there is a weak dynamic coupling between the PV system and the distribution network. Thus, an otherwise stable PV system does not destabilize the distribution network or itself when it is connected to a distribution network;
- the proposed control strategy enables the control/maximization of the PV system output power. It also enables the operation of the PV system at different power factor including the unity power-factor;
- the modal analysis indicates that, under proposed control strategy, the load type has no appreciable impact on dynamic properties of the PV system and

those of the overall system; and

- the modal analysis further confirmed that the PV system dynamics are not influenced by the distribution line length, the line X/R ratio, and the distance between the loads and the PV system.

6.2 Recommended Future Work

The following topics are suggested for future research in this area:

- the islanding behavior of the PV system under proposed control strategy is worth investigating in a future research. Thus, the adoption and incorporation of a suitable islanding detection scheme may be necessary in a practical system;
- a more detailed analysis and examination of the PV system behavior under faults is suggested. The result would be of interest to distribution system planners and utility companies; and
- the developed model can be augmented with a Maximum Power-Point Tracking (MPPT) strategy, and the model analysis repeated to investigate the impact of MPPT scheme on the PV system dynamics.

Appendices

Appendix A

System Parameters

The Parameters of the PV system, distribution line, induction machine, series $R-L$ load, and rectifier load are presented in Tables A.1-A.6.

Table A.1: PV System Parameters

Parameter	Value	Comments
$Tr1$ nominal power	1.7 MVA	
$Tr1$ voltage ratio	6.6/0.48 kV	Y/Delta
$Tr1$ leakage inductance	0.1 pu	
on-state resistance of valves	3 $m\Omega$	
interface inductance, L	100 μH	
interface resistance, R	3.0 $m\Omega$	
filter capacitance, C_f	300 μF	
switching frequency	3060 Hz	51× 60 Hz
DC-link capacitance, C	5000 μF	
# of PV cells per string, n_s	1500	
# of PV strings, n_p	176	
ideality factor, A	1.92	
temperature coefficient, k_θ	0.0017 A/K	
cell short circuit current, I_{scr}	8.03 A	at $T_r = 300\ K$
reverse saturation current, I_{rs}	$1.2 \times 10^{-7}\ A$	

Table A.2: Controller Parameters

Parameter	Value	Comments
k_p (for $\tau_i = 0.5\ ms$)	0.2 Ω	
k_i (for $\tau_i = 0.5\ ms$)	0.6 Ωs^{-1}	
β_1	307.3 $1/Vs^2$	
β_2	202.9 $1/Vs^3$	
β_3	600 s^{-1}	
α_1	-0.77 As^{-1}/V^2	
α_2	-328.2 As^{-2}/V^2	
α_3	909 s^{-1}	

Table A.3: Distribution Line Parameters

Parameter	Value	Comments
grid voltage	6.6 $kVrms$	$l-l$
line inductance, $L_1 + L_2$	0.105 mH per km	
X/R ratio	0.6	
line resistance	based on L & X/R	
line length, l_e	15 km	

Table A.4: Induction Machine Parametrs

Parameter	Value	Comments
nominal power	373 kVA	
nominal voltage	6.6 $kVrms$	$l-l$
nominal frequency	60 Hz	
rotor/stator turns ratio	1.0	
stator resistance, R_s	0.0184 pu	
rotor resistance, R_r	0.0132 pu	
magnetizing inductance, L_m	3.8 pu	
stator leakage factor, σ_s	0.0223	
rotor leakage factor, σ_r	0.0223	
inertia constant, H	2.1 s	
mechanical damping, D	0.135 pu	

Table A.5: $R-L$ Load Parametrs

Parameter	Value	Comments
nominal power	373 kVA	
nominal voltage	6.6 $kVrms$	$l-l$
Inductance, L_1	95 mH	
Resistance, R	111 Ω	
Power Factor	0.95	

Table A.6: Rectifier Load Parameters

Parameter	Value	Comments
nominal power	373 kVA	
nominal voltage	6.6 $kVrms$	$l-l$
DC Inductance, L_{rec}	2.0 H	
DC Resistance, R_{rec}	212 Ω	

Appendix B

PV System Start-Up and Normal Operation for series R-L load and Rectifier Load

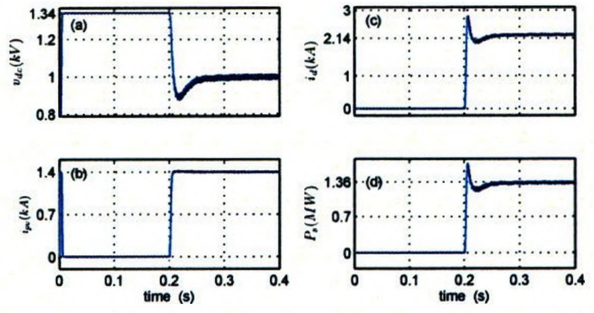

Figure B.1: PV system transient response during the start-up process with series $R-L$ load

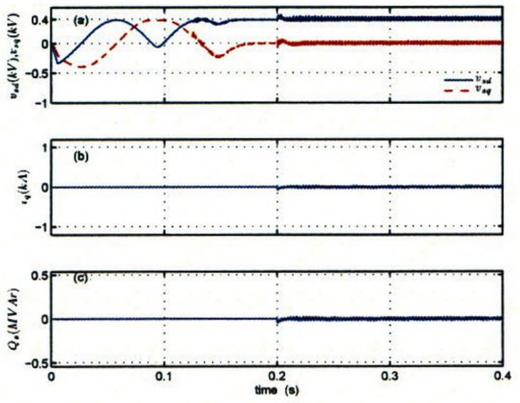

Figure B.2: PV system transient response during the start-up process with series $R-L$ load

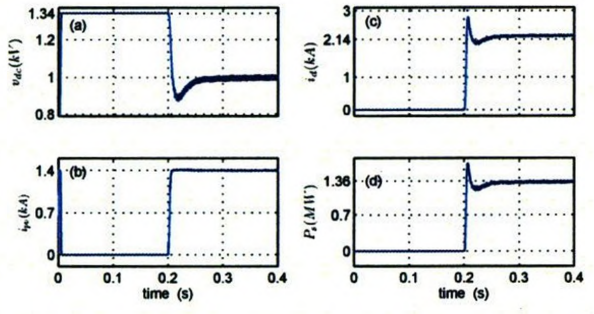

Figure B.3: PV system transient response during the start-up process with rectifier load

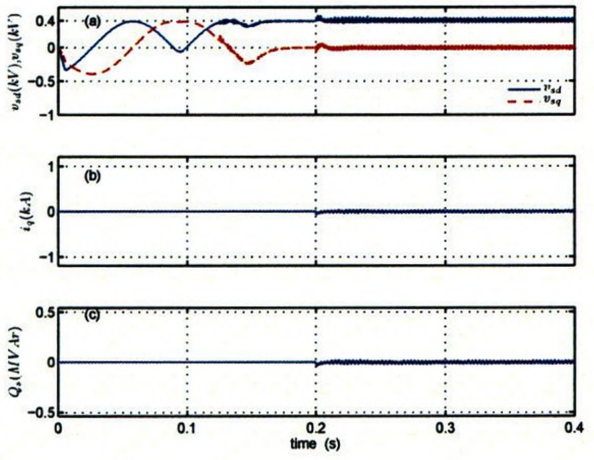

Figure B.4: PV system transient response during the start-up process with rectifier load

Appendix C

Linearized Equations of the PV Subsystem

the closed-loop transfer functions of d- and q-axis current controllers are,

$$\frac{I_d}{I_{dref}} = \frac{1}{\tau_i s + 1} \tag{C.1}$$

$$\frac{I_q}{I_{qref}} = \frac{1}{\tau_i s + 1} \tag{C.2}$$

Equations (C.1) and (C.2) can be written in time-domain form as follows,

$$\frac{di_d}{dt} = -\frac{1}{\tau_i} i_d + \frac{1}{\tau_i} i_{dref} \tag{C.3}$$

$$\frac{di_q}{dt} = -\frac{1}{\tau_i} i_q + \frac{1}{\tau_i} i_{qref} \tag{C.4}$$

If a small perturbation around steady-state is assumed, then the final perturbed state is

$$\frac{d\left(i_{d0} + \tilde{i}_d\right)}{dt} = -\frac{1}{\tau_i}(i_{d0} + \tilde{i}_d) + \frac{1}{\tau_i}(i_{dref0} + \tilde{i}_{dref}) \tag{C.5}$$

$$\frac{d\left(i_{q0} + \tilde{i}_q\right)}{dt} = -\frac{1}{\tau_i}(i_{q0} + \tilde{i}_q) + \frac{1}{\tau_i}(i_{qref0} + \tilde{i}_{qref}) \tag{C.6}$$

Equalizing the perturbed form on the left hand side and right hand side of equations (C.5) and (C.6) one deduces,

$$\frac{d\tilde{i}_d}{dt} = -\frac{1}{\tau_i}\tilde{i}_d \ominus \frac{1}{\tau_i}\tilde{i}_{dref} \tag{C.7}$$

$$\frac{d\tilde{i}_q}{dt} = -\frac{1}{\tau_i}\tilde{i}_q \ominus \frac{1}{\tau_i}\tilde{i}_{qref} \tag{C.8}$$

$$i_{dref} = \pounds^{-1}\{k_v(s)\} \star \left\{v_{dcref}^2 - v_{dc}^2\right\} + \gamma\frac{i_{pv}v_{dc}}{\frac{3}{2}v_{sd}} \tag{C.9}$$

Assuming a small perturbation around the steady-state, i_{dref0}, one obtains,

$$i_{dref0} + \tilde{i}_{dref} = \pounds^{-1}\{k_v(s)\} \star \left\{\left(v_{dcref0} + \tilde{v}_{dcref}\right)^2 - \left(v_{dc0} + \tilde{v}_{dc}\right)^2\right\} + \gamma\frac{\left(i_{pv0} + \tilde{i}_{pv}\right)\left(v_{dc0} + \tilde{v}_{dc}\right)}{\frac{3}{2}\left(v_{sd0} + \tilde{v}_{sd}\right)} \tag{C.10}$$

Equation C.10 can further be simplified to

$$i_{dref0} + \tilde{i}_{dref} = \pounds^{-1}\{k_v(s)\} \star \left\{\left(v_{dcref0} + \tilde{v}_{dcref}\right)^2 - \left(v_{dc0} + \tilde{v}_{dc}\right)^2\right\} + \gamma\frac{2\left(i_{pv0} + \tilde{i}_{pv}\right)\left(v_{dc0} + \tilde{v}_{dc}\right)}{3v_{sd0}}\left(1 - \frac{\tilde{v}_{sd}}{v_{sd0}}\right) \tag{C.11}$$

Neglecting second and higher-order terms of $\tilde{v}_{dcref}$ and $\tilde{v}_{dc}$,as well as the product $\tilde{i}_{pv}\tilde{v}_{dc}$, and equalizing the perturbed states of the both sides of Equation (C.10), one deduces

$$\tilde{i}_{dref} = \pounds^{-1}\{k_v(s)\} \star \left\{2v_{dcref0}\tilde{v}_{dcref} - 2v_{dc0}\tilde{v}_{dc}\right\} + \gamma\frac{i_{pv0}\tilde{v}_{dc}}{\frac{3}{2}v_{sd0}} + \gamma\frac{v_{dc0}\tilde{i}_{pv}}{\frac{3}{2}v_{sd0}} \ominus \gamma\frac{2i_{pv0}v_{dc0}\tilde{v}_{sd}}{3v_{sd0}^2} \tag{C.12}$$

Defining $\tilde{u}_1 = 2v_{dcref0}\tilde{v}_{dcref}$, $\tilde{u}_4 = \tilde{v}_{sd}$, and $\tilde{x}_2 = 2v_{dc0}\tilde{v}_{dc}$ Equation (C.12) is re-written as,

$$\tilde{i}_{dref} == \pounds^{-1}\{k_v(s)\} \star \{\tilde{u}_1 - \tilde{x}_2\} + \gamma\frac{I_{pv0}\tilde{x}_2}{3v_{sd0}v_{dc0}} + \gamma\frac{2v_{dc0}\tilde{i}_{pv}}{3v_{sd0}} + \gamma\frac{2i_{pv0}v_{dc0}}{3v_{sd0}^2}\tilde{u}_4 \quad (C.13)$$

substituting for $k_v(s) = \frac{\alpha_1 s+\alpha_2}{s(s+\alpha_3)}$ in (C.13), one finds

$$\tilde{i}_{dref} = \pounds^{-1}\left\{\frac{\alpha_1 s + \alpha_2}{s(s+\alpha_3)}\right\} \star (\tilde{u}_1 - \tilde{x}_2) + \gamma\frac{i_{pv0}\tilde{x}_2}{3v_{sd0}v_{dc0}} + \gamma\frac{2v_{dc0}\tilde{i}_{pv}}{3v_{sd0}} + \gamma\frac{2i_{pv0}v_{dc0}}{3v_{sd0}^2}\tilde{u}_4. \quad (C.14)$$

Let us define

$$\tilde{X}_3 = \frac{\left(\tilde{U}_1 - \tilde{X}_2\right)}{s(s+\alpha_3)} \quad (C.15)$$

and

$$\frac{d\tilde{x}_3}{dt} = \tilde{x}_4 \quad (C.16)$$

then

$$\frac{d\tilde{x}_4}{dt} = -\alpha_3\tilde{x}_4 - \tilde{x}_2 + \tilde{u}_1. \quad (C.17)$$

Moreover, (C.14) can be rewritten as:

$$\tilde{i}_{dref} = \alpha_1\tilde{x}_4 + \alpha_2\tilde{x}_3 + \gamma\frac{i_{pv0}}{3v_{sd0}v_{dc0}}\tilde{x}_2 + \gamma\frac{2v_{dc0}}{3v_{sd0}}\tilde{i}_{pv} + \gamma\frac{2i_{pv0}v_{dc0}}{3v_{sd0}^2}\tilde{u}_4 \quad (C.18)$$

To find an expression for $\tilde{i}_{pv}$, (2.1) is perturbed around the steady-state point. Thus,

$$i_{pv0} + \tilde{i}_{pv} = n_p I_{scr}(S_0 + \tilde{S}) - n_p I_{rs}\left\{\left[\exp\left(\frac{q}{kTA}(v_{dc0} + \tilde{v}_{dc})\right)\right] - 1\right\} \quad (C.19)$$

The exponential term of (C.19) can be expanded using Taylor's series expansion. Thus, neglecting second and higher order term (C.19) is simplified to

$$\tilde{i}_{pv} = I_{scr}\tilde{S} - n_p I_{rs}\left(\frac{q}{kTA}\tilde{v}_{dc}\right) \tag{C.20}$$

Introducing $\mu = n_p I_{rs}(\frac{q}{kTA})$ and multiplying both sides of (C.20) by $2v_{dc0}$ one obtains,

$$\tilde{i}_{pv} = I_{scr}\tilde{S} - \frac{\mu}{2v_{dc0}}\tilde{X}_2 \tag{C.21}$$

Substituting for $\tilde{i}_{pv}$ in (C.18), i_{dref} assumes the form:

$$\tilde{i}_{dref} = \alpha_1\tilde{x}_4 + \alpha_2\tilde{x}_3 + \gamma\frac{i_{pv0}}{3v_{sd0}v_{dc0}}\tilde{x}_2 - \gamma\frac{\mu}{3v_{sd0}}\tilde{x}_2 + I_{scr}\tilde{S} + \gamma\frac{2i_{pv0}v_{dc0}}{3v_{sd0}^2}\tilde{u}_4. \tag{C.22}$$

Substituting for $\tilde{i}_{dref}$ in (C.7) and defining $\tilde{x}_1 = \tilde{i}_d$ and $\tilde{u}_2 = \tilde{S}$ it becomes

$$\frac{d\tilde{x}_1}{dt} = -\frac{1}{\tau_i}\tilde{x}_1 + \gamma\frac{i_{pv0}}{3v_{sd0}v_{dc0}\tau_i}\tilde{x}_2 - \gamma\frac{\mu}{3v_{sd0}\tau_i}\tilde{x}_2 + \frac{1}{\tau_i}\alpha_2\tilde{x}_3 + \frac{1}{\tau_i}\alpha_1\tilde{x}_4 + \frac{I_{scr}}{\tau}\tilde{u}_2 - \gamma\frac{2i_{pv0}v_{dc0}}{3\tau_i v_{sd0}^2}\tilde{u}_4 \tag{C.23}$$

Similarly, introducing $\tilde{i}_q = \tilde{x}_5$ and $\tilde{i}_{qref} = \tilde{u}_3$, (C.8) can be re-written as:

$$\frac{d\tilde{x}_5}{dt} = -\frac{1}{\tau_i}\tilde{x}_5 - \frac{1}{\tau_i}\tilde{u}_3 \tag{C.24}$$

A linearized dynamic model of the DC-link voltage, based on (2.18), is derived as:

$$\begin{aligned}\frac{C}{2}\frac{d}{dt}(v_{dc0}+\tilde{v}_{dc})^2 = {} & \left(i_{pv0}+\tilde{i}_{pv}\right)(v_{dc0}+\tilde{v}_{dc}) - \frac{3}{2}\left(i_{d0}+\tilde{i}_d\right)(v_{sd0}+\tilde{v}_{sd}) \\ & -\frac{3}{2}\left(i_{q0}+\tilde{i}_q\right)\left(v_{sq0}+\tilde{v}_{sq}\right) - \frac{3L}{2}\left(i_{d0}+\tilde{i}_d\right)\frac{d}{dt}\left(i_{d0}+\tilde{i}_d\right) \\ & -\frac{3L}{2}\left(i_{q0}+\tilde{i}_q\right)\frac{d}{dt}\left(i_{q0}+\tilde{i}_q\right) - \frac{3R}{2}\left(i_{d0}+\tilde{i}_d\right)^2 \\ & -\frac{3R}{2}\left(i_{q0}+\tilde{i}_q\right)^2\end{aligned} \tag{C.25}$$

Introducing $\tilde{u}_5 = \tilde{v}_{sq}$ neglecting the second- and higher-order terms of $\tilde{i}_d$, $\tilde{i}_q$, and neglecting the products $\tilde{i}_{pv}\tilde{v}_{dc}$, and $\tilde{i}_d\tilde{v}_{sd}$, $\tilde{i}_q\tilde{v}_{sq}$, (C.25) can be simplified as:

$$\begin{aligned}\frac{C}{2}\frac{d\tilde{x}_2}{dt} = &-\frac{3}{2}v_{sd0}\tilde{x}_1 - \frac{3L}{2}i_{d0}\frac{d\tilde{x}_1}{dt} - 3Ri_{d0}\tilde{x}_1 \\ &+\frac{i_{pv0}}{2v_{dc0}}\tilde{x}_2 + v_{dc0}\tilde{i}_{pv} - 3Ri_{q0}\tilde{x}_5 - \frac{3}{2}v_{sq0}\tilde{x}_5 - \frac{3L}{2}i_{q0}\frac{d\tilde{x}_5}{dt} \\ &-\frac{3}{2}i_{d0}\tilde{u}_4 - \frac{3}{2}i_{q0}\tilde{u}_5 \end{aligned} \quad \text{(C.26)}$$

Equation (C.26) can be expressed in terms of $\tilde{x}_1$, $\tilde{x}_2$, $\tilde{x}_3$, $\tilde{x}_4$, and $\tilde{x}_5$ by substitution of $\tilde{i}_{pv}$, $\frac{d\tilde{x}_1}{dt}$, and $\frac{d\tilde{x}_5}{dt}$ from (C.21), (C.23) and (C.24). Thus,

$$\begin{aligned}\frac{C}{2}\frac{d\tilde{x}_2}{dt} = &-\frac{3}{2}v_{sd0}\tilde{x}_1 + \frac{3Li_{d0}}{2\tau_i}\tilde{x}_1 - 3Ri_{d0}\tilde{x}_1 + \frac{i_{pv0}}{2v_{dc0}}\tilde{x}_2 - \frac{\mu}{2}\tilde{x}_2 \\ &-\gamma\frac{Li_{d0}}{2v_{sd}\tau_i}\tilde{x}_2 - \gamma\frac{i_{pv0}Li_{d0}}{2v_{sd0}v_{dc0}\tau_i}\tilde{x}_2 - \frac{3Li_{d0}\alpha_2}{2\tau_i}\tilde{x}_3 - \frac{3Li_{d0}\alpha_1}{2\tau_i}\tilde{x}_4 \\ &-\frac{3}{2}v_{sq0}\tilde{x}_5 + \frac{3Li_{q0}}{2\tau_i}\tilde{x}_5 - 3Ri_{q0}\tilde{x}_5 + v_{dc0}I_{scr}\tilde{u}_2 + \frac{3L}{2\tau_i}\tilde{u}_3 \\ &-\gamma\frac{Li_{pv0}v_{dc0}}{\tau_i v_{sd0}^2}\tilde{u}_4 - \frac{3}{2}i_{d0}\tilde{u}_4 - \frac{3}{2}i_{q0}\tilde{u}_5 \end{aligned} \quad \text{(C.27)}$$

Multiplying the both sides of (C.27) by $2/C$, one deduces:

$$\begin{aligned}\frac{d\tilde{x}_2}{dt} = &-\frac{3}{C}v_{sd0}\tilde{x}_1 + \frac{3Li_{d0}}{C\tau_i}\tilde{x}_1 - \frac{6Ri_{d0}}{C}\tilde{x}_1 + \frac{i_{pv0}}{Cv_{dc0}}\tilde{x}_2 - \frac{\mu}{C}\tilde{x}_2 - \gamma\frac{Li_{d0}}{Cv_{sd}\tau_i}\tilde{x}_2 \\ &-\gamma\frac{i_{pv0}Li_{d0}}{Cv_{sd0}v_{dc0}\tau_i}\tilde{x}_2 - \frac{3Li_{d0}\alpha_2}{C\tau_i}\tilde{x}_3 - \frac{3Li_{d0}\alpha_1}{C\tau_i}\tilde{x}_4 \\ &-\frac{3}{C}v_{sq0}\tilde{x}_5 + \frac{3Li_{q0}}{C\tau_i}\tilde{x}_5 - \frac{6Ri_{q0}}{C}\tilde{x}_5 + \frac{2v_{dc0}I_{scr}}{C}\tilde{u}_2 \\ &+\frac{2v_{dc0}I_{scr}}{C}\tilde{u}_2 - \frac{3}{C}i_{d0}\tilde{u}_3 - \frac{3}{C}i_{d0}\tilde{u}_4 - \gamma\frac{2Li_{pv0}v_{dc0}}{C\tau_i v_{sd0}^2}\tilde{u}_4 - \frac{3}{C}i_{q0}\tilde{u}_5 \end{aligned} \quad \text{(C.28)}$$

The PLL linearized equations assume the forms:

$$\frac{d\tilde{x}_6}{dt} = -\beta_3\tilde{x}_1 + \tilde{v}_{sq}\,(=\tilde{u}_5) \quad \text{(C.29)}$$

$$\frac{d\tilde{x}_7}{dt} = \tilde{x}_6 \tag{C.30}$$

$$\frac{d\tilde{\rho}}{dt} = \beta_1 \tilde{x}_6 + \beta_2 \tilde{x}_7. \tag{C.31}$$

Appendix D

Linearized Equations of the Distribution Network Subsystem

$$\frac{d\tilde{i}_{g1d}}{dt} = -\frac{R_1}{L_1}\tilde{i}_{g1d} + \omega_0\tilde{i}_{g1q} + \frac{N}{L_1}\tilde{v}_{sd} - \frac{1}{L_1}\tilde{v}_{ld} + \tilde{\omega}i_{g1q0} \tag{D.1}$$

$$\frac{d\tilde{i}_{g1q}}{dt} = -\omega_0\tilde{i}_{g1d} - \frac{R_1}{L_1}\tilde{i}_{g1q} + \frac{N}{L_1}\tilde{v}_{sq} - \frac{1}{L_1}\tilde{v}_{lq} - \tilde{\omega}i_{g1d0} \tag{D.2}$$

$$\frac{d\tilde{i}_{g2d}}{dt} = -\frac{R_2}{L_2}\tilde{i}_{g2d} + \omega_0\tilde{i}_{g2q} + \frac{1}{L_2}\tilde{v}_{ld} + \frac{1}{L_2}\hat{v}_g \sin\theta_0\tilde{\theta} + \tilde{\omega}i_{g2q0} \tag{D.3}$$

$$\frac{d\tilde{i}_{g2q}}{dt} = -\omega_0\tilde{i}_{g2d} - \frac{R_2}{L_2}\tilde{i}_{g2q} + \frac{1}{L_2}\tilde{v}_{lq} + \frac{1}{L_2}\hat{v}_g \cos\theta_0\tilde{\theta} + \tilde{\omega}i_{g2q0} \tag{D.4}$$

$$\frac{d\tilde{v}_{sd}}{dt} = \frac{1}{c_f}\tilde{i}_d - \frac{N}{c_f}\tilde{i}_{g1d} + \omega_0\tilde{v}_{sq} + v_{sq0}\tilde{\omega} \tag{D.5}$$

$$\frac{d\tilde{v}_{sq}}{dt} = \frac{1}{c_f}\tilde{i}_q - \frac{N}{c_f}\tilde{i}_{g1q} - \omega_0\tilde{v}_{sd} - v_{sd0}\tilde{\omega} \tag{D.6}$$

$$\frac{d\tilde{v}_{ld}}{dt} = \frac{1}{c_l}\tilde{i}_{g1d} - \frac{1}{c_l}\tilde{i}_{g2d} + \omega_0\tilde{v}_{lq} - \frac{1}{c_l}\tilde{i}_{ld} + v_{lq0}\tilde{\omega} \tag{D.7}$$

$$\frac{d\tilde{v}_{lq}}{dt} = \frac{1}{c_l}\tilde{i}_{g1q} - \frac{1}{c_l}\tilde{i}_{g2q} - \omega_0\tilde{v}_{ld} - \frac{1}{c_l}\tilde{i}_{lq} + v_{lq0}\tilde{\omega} \tag{D.8}$$

Appendix E

Linearized Equations of the Load Subsystem

$$\frac{d\tilde{i}_{1d}}{dt} = -\frac{(1+\sigma_r)}{(1+\sigma_r)(1+\sigma_s)-1}\frac{R_s}{L_m}\tilde{i}_{1d} + \omega_0\tilde{i}_{1q} + \frac{1}{(1+\sigma_r)(1+\sigma_s)-1}\frac{R_r}{L_m}\tilde{i}_{2d} + \frac{1}{L_m}\tilde{v}_{ld} + \tilde{i}_{1q0}\tilde{\omega} \tag{E.1}$$

$$\frac{d\tilde{i}_{1q}}{dt} = -\omega_0\tilde{i}_{1d} - \frac{(1+\sigma_r)}{(1+\sigma_r)(1+\sigma_s)-1}\frac{R_s}{L_m}\tilde{i}_{1q} + \frac{1}{(1+\sigma_r)(1+\sigma_s)-1}\frac{R_r}{L_m}\tilde{i}_{2q} + \frac{1}{L_m}\tilde{v}_{lq} \tag{E.2}$$

$$\frac{d\tilde{i}_{2d}}{dt} = \frac{1}{(1+\sigma_r)(1+\sigma_s)-1}\frac{R_r}{L_m}\tilde{i}_{1d} - \frac{(1+\sigma_s)}{(1+\sigma_r)(1+\sigma_s)-1}\frac{R_r}{L_m}\tilde{i}_{2d} + (\omega_0-\omega_{r0})\tilde{i}_{2q} + i_{2q0}\tilde{\omega}_r - i_{2q0}\tilde{\omega} \tag{E.3}$$

$$\frac{d\tilde{i}_{2q}}{dt} = \frac{1}{(1+\sigma_r)(1+\sigma_s)-1}\frac{R_r}{L_m}\tilde{i}_{1q} - \frac{(1+\sigma_s)}{(1+\sigma_r)(1+\sigma_s)-1}\frac{R_r}{L_m}\tilde{i}_{2q} - (\omega_0-\omega_{r0})\tilde{i}_{2d} + i_{2d0}\tilde{\omega}_r - i_{2d0}\tilde{\omega} \tag{E.4}$$

$$\frac{d\tilde{\omega}_r}{dt} = -\frac{3L_m i_{2q0}}{2J\left[(1+\sigma_r)(1+\sigma_s)-1\right]}\tilde{i}_{1d} + \frac{3L_m i_{2d0}}{2J\left[(1+\sigma_r)(1+\sigma_s)-1\right]}\tilde{i}_{2q}$$
$$+\frac{3L_m i_{1q0}}{2J\left[(1+\sigma_r)(1+\sigma_s)-1\right]}\tilde{i}_{2d} - \frac{3L_m i_{1d0}}{2J\left[(1+\sigma_r)(1+\sigma_s)-1\right]} - \frac{D}{J}\tilde{\omega}_r - \frac{\tilde{T}_m}{J} \quad \text{(E.5)}$$

References

[1] H. L. Willis and W.G. Scott, *Distributed power generation: planning and evaluation* Marcel Dekker, New York, 2000.

[2] M. Oprisan and S. Pneumaticos, "Potential for electricity generation from emerging renewable sources in Canada," *IEEE EIC Climate Change Technology Conference 2006*, pp. 1-9, May 2006.

[3] Royal Commission of Environmental Pollution's 22nd report: Energy-The changing Climate, pp. 251-262, June 2000. Appendix E.

[4] G.M. Masters, "Renewable and efficient electric power system," Wiley Interscience, 2005.

[5] J. J. Bzura, "The New England electric photovoltaic systems research and demonstration project," *IEEE Transactions on Energy Conversion*, vol. 5, no. 2, pp. 284-289, June 1990.

[6] J. J. Bzura, "Performance of grid-connected photovoltaic systems on residences and commercial buildings in New Engalnd," *IEEE Transactions on Energy Conversion*, vol. 7, no. 1, pp. 79-82, March 1992.

[7] I. Abouzahr and R. Ramakumar, "An approach to assess the performance of utility-interactive photovoltaic systems," *IEEE Transactions on Energy Conversion*, vol. 8, no. 2, pp. 145-153, June 1993.

[8] T. Esram and P.L. Chapman, "Comparison of photovoltaic array maximum power point tracking techniques," *IEEE Transactions on Energy Conversion*, vol. 22, pp. 434-449, June 2007.

[9] H. Haeberlin, "Evolution of inverters for grid connected PV systems from 1989 to 2000," *Proceedings of Photovoltaic Solar Energy Conference*, pp. 426-430, 2001.

[10] S. B. Kjaer, J. K. pedersen and F. Blaabjerg, "A review of single-phase grid-connected inverters for photovoltaic modules," *IEEE Transactions on Industry Applications*, vol. 41, no. 5, pp. 1292-1306, Sep./Oct. 2005.

[11] Y. Huang, F. Z. Peng, J. Wang and D. Yoo "Survey of power conditioning system for PV power generation," *Power Electronics Specialist Conference*, PESC 2006, 6 pages, June 2006.

[12] J. M. Carrasco, L. G. Franquelo, J. T. Bialasiewicz, E. Galvan, R. C. PortilloGuisado, M. A. M. Prats, J.I. Leon, N. Moreno-Alfonso, "Power-electronic systems for the grid integration of renewable energy sources: a survey," *IEEE Transactions on Industrial Electronics*, vol. 53, no. 4, pp. 1002-1016, August 2006.

[13] G. Kern, "SunSine300: utility interactive ac module anti-islanding test results," *Proceedings of IEEE Photovoltaic Specialists Conference*, pp. 1265-1268, 1997.

[14] Y. Noda, T. Mizuno, H. Koizumi, K. Nagasaka and K. Kurokawa, "The development of a scaled-down simulator for distribution grids and its application for veryfying interference behavior among a number of module integrated converters (MIC)," *Proceedings of IEEE Photovoltaic Specialists Conference*, pp. 1545-1548, May 2002.

[15] A. Woyte, R. Belmans and N. Nijs, "Testing and islanding protection function of photovoltaic inverters," *IEEE Transactions on Energy Conversion*, vol. 18, no. 1, pp. 157-162, March 2003.

[16] L. A. C. Lopes and H. Sun, "Performance assessment of active frequency drifting islanding detection methods," *IEEE Transactions on Energy Conversion*, pp. 171-180, March 2006.

[17] G. L. Campen, "An analysis of the harmonics and power factor effects at a utility intertied photovoltaic system," *IEEE Transaction on Power Apparatus and Systems*, vol. PAS 101, pp. 4632-4639, December 1982.

[18] J. H. R. Enslin and P. J. M. Heskes, "Harmonic interaction between a large number of distributed power inverters and the distribution network," *IEEE Transactions on Power Electronics*, vol. 19, no. 6, pp. 1586-1593, November 2004.

[19] M. C. Benhabib, J. M. A. Myrzik and J. L. Duarte, "Harmonic effects caused by large scale PV installations in LV network," *International Conferenve on Electrical Power Quality and Utilization, EPQU 2007*, 6 pages, October 2007.

[20] N. Srisaen and A. Sangswang, "Effect of pv grid-connected system location on a distribution system," *IEEE Asia Pacific Conference on Circuit and Systems, APCCAS 2006*, pp. 852-855, December 2006.

[21] A. Woyte, V. Van Thong, R. Belmans and J. Nijs, "Voltage fluctuations on distribution level introduced by photovoltaic systems," *IEEE Transactions on Energy Conversion*, vol. 21, no.1, pp. 202-209, March 2006.

[22] M. Thomson and D.G. Infield, "Impact of widespread photovoltaics generation on distribution systems," *IET Journal of Renewable Power Generation*, vol. 1, no. 1, pp. 33-40, March 2007.

[23] L. Wang and Y. Lin, "Dynamic Stability analysis of photovoltaic array connected to a large utility grid," *IEEE Power Engineering Society Winter Meeting 2000*, vol. 1, pp. 476-480, January 2000.

[24] M. Liserre, R Teodorescue and F. Blaabjerg, "Stability of photovoltaic and wind turbine grid-connected inverters for a large set of grid impedance values," *IEEE Transactions on Power Electronics*, vol. 21, no. 1, pp. 263-272, January 2006.

[25] B. Rodriguez and G. A. J. Amartunga, "Dynamic stability of grid-connected photovoltaic systems," *IEEE Power Engineering Society General Meeting*, PES 2004, vol. 2, pp. 2193-2199, June 2004.

[26] T. Ostrem, W. Sulkowski, L. E. Norum and C. Wang, "Grid connected photovoltaic (PV) inverter with robust phase-locked loop (PLL)," *IEEE/PES Transmission and Distribution Conference and Exposition, TDC 06*, 7 pages, August 2006.

[27] O. Wasynczuk and N. A. Anwah, "Modeling and dynamic performance of a self-commutated photovoltaic inverter system," *IEEE Transactions on Energy Conversion*, vol. 4, no. 3, pp. 322-328, September 1989.

[28] S. Zheng, P. Wang and L Ge, "Study on pwm control strategy of photovoltaic grid-connected generation system," *IEEE International Conference on Power Electronics and Motion Control, IPEMC 06*, vol. 3, 5 pages, August 2006.

[29] E. Figueres, G. Garcera, J. Sandia, F. J. Gonzalez-Espin, "Modelling and control of a 100 kW photovoltaic inverter with an LCL grid filter for distributed power systems," *European Conference on Power Electronics and Applications*, 10 pages, September 2007.

[30] W. Libo, Z. Zhengming and L. Jianzheng, "A single-stage three phase grid-connected photovoltaic system with modified MPPT method and reactive power compensation," *IEEE Transactions on Energy Conversion*, vol. 22, no. 4, pp-881-886, December 2007.

[31] PSCAD/EMTDC v. 4.2, Manitoba HVDC Research Centre, Winnipeg, MB, Canada.

[32] K. H. Hussein, I. Muta, T. Hoshino and M. Osakada, "Maximum photovoltaic power tracking: an algorithm for rapidly changing atmospheric conditions," *IEE Proceedings on Generation, Transmission, and Distribution*, vol. 142, no. 1, pp. 59-64, January 1995.

[33] P. Vas, *Vector Control of AC Machines*, Oxford University Press, 1990.

[34] A. Yazdani and R. Iravani, "An accurate model for the dc-side voltage control of the neutral point diode clamped converter," *IEEE Trans. On Power Delivery*, vol. 21, no. 1, pp. 185-193, January 2006.

[35] S. K. Chung, "A phase tracking system for three phase utility interface inverters," *IEEE Transactions on Power Electronics*, vol. 15, no. 3, pp. 431-438, May 2000.

[36] C. Schauder and H. Mehta, "Vector analysis and control of advanced static VAR compensators," *IEE Proceedings – Generation, Transmission, and Distribution*, vol. 140, no. 4, pp. 299-306, July 1993.

[37] W. Leonhard, *Control of Electrical Drives*, Springer, 3rd ed., 2001.

[38] P. Kundur, *Power System Stability and Control*, McGraw Hill, 1994.

[39] H. K. Khalil, *Nonlinear Systems*, Printice Hall, 2001

[40] E.E.S. Lima, "A sensitivity analysis of eigenstructure in power system dynamic stability," *IEEE Transaction on Power System*, vol. 12, no. 3, pp. 1393-1399, August 1997.

[41] B. Porter and T. R. Crossley, *Modal Control: Theory and Applications*, Taylor & Francis Ltd., London, 1972.

[42] K. Thorborg, *Power Electronics*, Prentice Hall, 1988.